Acta Pharmaceutica Sinica B 2023;13(12):5030–5047

Chinese Pharmaceutical Association
Institute of Materia Medica, Chinese Academy of Medical Sciences

Acta Pharmaceutica Sinica B

www.elsevier.com/locate/apsb
www.sciencedirect.com

ORIGINAL ARTICLE

Remodeling of the liver fibrosis microenvironment based on nilotinib-loaded multicatalytic nanozymes with boosted antifibrogenic activity

Huaqing Jing[a], Yingzi Ren[a], Yue Zhou[a], Min Xu[a], Sona Krizkova[b], Zbynek Heger[b], Qiang Lu[a], Siyu Wang[a], Xiaoyang Liang[a], Vojtech Adam[b,*], Nan Li[a,*]

[a]*Tianjin Key Laboratory of Drug Delivery & High-Efficiency, School of Pharmaceutical Science and Technology, Tianjin University, Tianjin 300072, China*
[b]*Department of Chemistry and Biochemistry, Mendel University in Brno, Brno 61300, Czech Republic*

Received 19 April 2023; received in revised form 7 July 2023; accepted 15 July 2023

KEY WORDS

Liver fibrosis;
Microenvironment remodeling;
HSCs;
ECM;
Collagen;
Hypoxia;
Nilotinib;
Nanozyme

Abstract Liver fibrosis is a reversible pathological process caused by chronic liver damage and a major risk factor for hepatocellular carcinoma (HCC). Hepatic stellate cell (HSC) activation is considered the main target for liver fibrosis therapy. However, the efficiency of this strategy is limited due to the complex microenvironment of liver fibrosis, including excessive extracellular matrix (ECM) deposition and hypoxia-induced imbalanced ECM metabolism. Herein, nilotinib (NIL)-loaded hyaluronic acid (HA)-coated Ag@Pt nanotriangular nanozymes (APNH NTs) were developed to inhibit HSCs activation and remodel the microenvironment of liver fibrosis. APNH NTs efficiently eliminated intrahepatic reactive oxygen species (ROS) due to their inherent superoxide dismutase (SOD) and catalase (CAT) activities, thereby downregulating the expression of NADPH oxidase-4 (NOX-4) and inhibiting HSCs activation. Simultaneously, the oxygen produced by the APNH NTs further alleviated the hypoxic microenvironment. Importantly, the released NIL promoted collagen depletion by suppressing the expression of tissue inhibitor of metalloproteinase-1 (TIMP-1), thus synergistically remodeling the microenvironment of liver fibrosis. Notably, an *in vivo* study in CCl_4-induced mice revealed that APNH NTs exhibited significant antifibrogenic effects without obvious long-term toxicity. Taken together, the data from this work suggest

*Corresponding authors.
E-mail addresses: vojtech.adam@mendelu.cz (Vojtech Adam), linan19850115@163.com (Nan Li).

Peer review under the responsibility of Chinese Pharmaceutical Association and Institute of Materia Medica, Chinese Academy of Medical Sciences.

https://doi.org/10.1016/j.apsb.2023.08.020

that treatment with the synthesized APNH NTs provides an enlightening strategy for remodeling the microenvironment of liver fibrosis with boosted antifibrogenic activity.

1. Introduction

Liver fibrosis is a dynamic and reversible wound-healing response to chronic liver injury. Various pathological factors, such as viral infections, alcohol abuse, autoimmune diseases, nonalcoholic fatty liver disease (NAFLD), and metabolic disorders, contribute to the development of liver fibrosis[1,2]. Chronic liver damage is usually accompanied by necrosis of hepatocytes and the release of cell contents, which trigger ROS-mediated oxidative stress, thereby further accelerating the progression of liver fibrosis[3,4]. If left untreated, liver fibrosis can further develop into cirrhosis, which is irreversible and can lead to HCC[5]. However, in clinical practice, there are no specific therapeutic options for the treatment of liver fibrosis other than traditional drugs that are frequently inefficient[6].

The main characteristic of liver fibrosis is excessive deposition of ECM and abnormal proliferation of intrahepatic connective tissue, which reflects the imbalance of repair and scar formation of the liver[7,8]. In particular, hypoxia is considered an important microenvironmental feature of liver fibrosis, which is involved in the development and progression of liver fibrosis by affecting the imbalance of ECM metabolism, mostly cross-linked collagen-I[9,10]. Furthermore, many studies have shown that HSCs play a prominent role in liver fibrosis and are the primary effector cells in fibrogenesis and major ECM-producing cells[11,12]. HSCs experience enhanced collagen accumulation due to the overexpression of TIMP-1, which can antagonize metalloproteinase activity to disrupt collagen depletion[13]. In recent decades, many chemical agents have shown potential antifibrogenic activity *in vitro* or *in vivo*[14]. For example, NIL has been studied extensively for its beneficial antifibrogenic effects by promoting collagen depletion through inhibition of TIMP-1[15,16]. However, the efficacy and clinical translation of NIL remain major challenges due to its poor solubility, low oral absorption, and limited liver-targeting efficiency[17]. Fortunately, the emerging discovery of nanodrugs has enabled their testing for specific drug delivery[18−23]. Thus, considering the pathogenesis of liver fibrosis, nanozymes with multiple catalytic functions capable of ROS elimination and hypoxia alleviation present a promising strategy for effective liver fibrosis therapy.

Recently, a plethora of inorganic nanomaterials have been investigated for possible use as nanocarriers for liver fibrosis therapy. Among these, Au, Ag or Pt nanoparticles (NPs), which exhibit good biocompatibility with negligible toxic side effects, have been exploited[24,25]. Interestingly, owing to the synergistic effect of two components, bimetallic nanoalloys tend to exhibit superior chemical properties and better catalytic performance than single-component NPs. For instance, bimetallic Ag@Pt NPs have been widely studied due to their high antioxidant efficiency and tailorable morphology[26]. Ag@Pt NPs can be prepared by a galvanic reaction in which Ag-forming NPs are partially displaced by Pt, which exhibits better catalytic activity and catalyst durability than pure Ag or Pt NPs[27]. In addition, controlled synthesis of Ag@Pt alloys can be achieved by using different Ag nanotemplates, such as spherical NPs, nanowires, and nanotubes. Compared to other shapes, triangular Ag@Pt NPs have many advantages, such as sharp vertices and edges, special local curvature and a large surface-to-volume ratio, showing enhanced cellular uptake and excellent SOD and CAT-like enzymomimetic activities[28].

Herein, we present a synergistic strategy for boosted antifibrogenic therapy based on NIL-loaded HA-modified triangular Ag@Pt nanozymes (Ag@Pt-NIL/HA nanotriangles, APNH NTs), which are able to remodel the microenvironment of liver fibrosis by hypoxia alleviation as well as collagen depletion to inhibit HSCs activation. As shown in Scheme 1, the therapeutic mechanism of APNH NTs encompasses i) a specific interaction between CD44, which is upregulated on the surface of HSCs, and HA on the APNH NTs, triggering CD44-mediated endocytosis and bioaccumulation in the lesion[29]; ii) the promotion of ROS elimination owing to the superb SOD and CAT-like activities, thus inhibiting HSCs activation by suppressing NOX-4 expression; and iii) the production of oxygen because the catalytic activity of APNH NTs overturns the hypoxic microenvironment of liver fibrosis. During this process, NIL is released from the APNH NTs in the acidic endo/lysosomal compartments and triggers collagen depletion by downregulating TIMP-1, therefore causing synergistic remodeling of the microenvironment of liver fibrosis.

2. Materials and methods

2.1. Materials and instrumentation

Silver nitrate ($AgNO_3$), sodium borohydride ($NaBH_4$) and polyvinylpyrrolidone (PVP, MW = 30,000) were bought from Yuanli Chemical Co., Ltd. (Tianjin China). Sodium citrate tribasic dihydrate, potassium tetrachloroplatinate (II) (K_2PtCl_4, 46.6% Pt), L-ascorbic acid (H_2ASc), HA (100 kDa), nilotinib (NIL, 98%), cysteine, 4-dimethylaminopyridine (DMAP), 1-ethyl-3-(3-dimethylaminopropyl)carbodiimide hydrochloride (EDC), fluorescein isothiocyanate (FITC), carbon tetrachloride (CCl_4) and olive oil were obtained from Heowns Science Co., Ltd. (Tianjin, China). Hydrogen peroxide (H_2O_2, 30 wt%) was bought from Aladdin Biochemical Technology Co., Ltd. (Shanghai, China). Cytotoxicity assay kit (CCK-8) was obtained from Labgic Co., Ltd. (Beijing, China). DMSO, 4′,6-diamidino-2-phenylindole (DAPI), Hoechst 33342, LysoTracker Red, Calcein/PI cell viability assay kit, PBS, lipopolysaccharide (LPS), ROS probe (2,7-dichlorodihydrofluorescein diacetate, DCFH-DA), hydrogen peroxide probe (ROS Green™ H_2O_2), superoxide anion probe (dihydrorethidium, DHE), Annexin V-FITC apoptosis detection kits, as well as SOD and CAT activity assay kits were all purchased from Solarbio Science & Technology Co., Ltd. (Beijing, China). ROS-ID™ hypoxia/oxidative stress detection

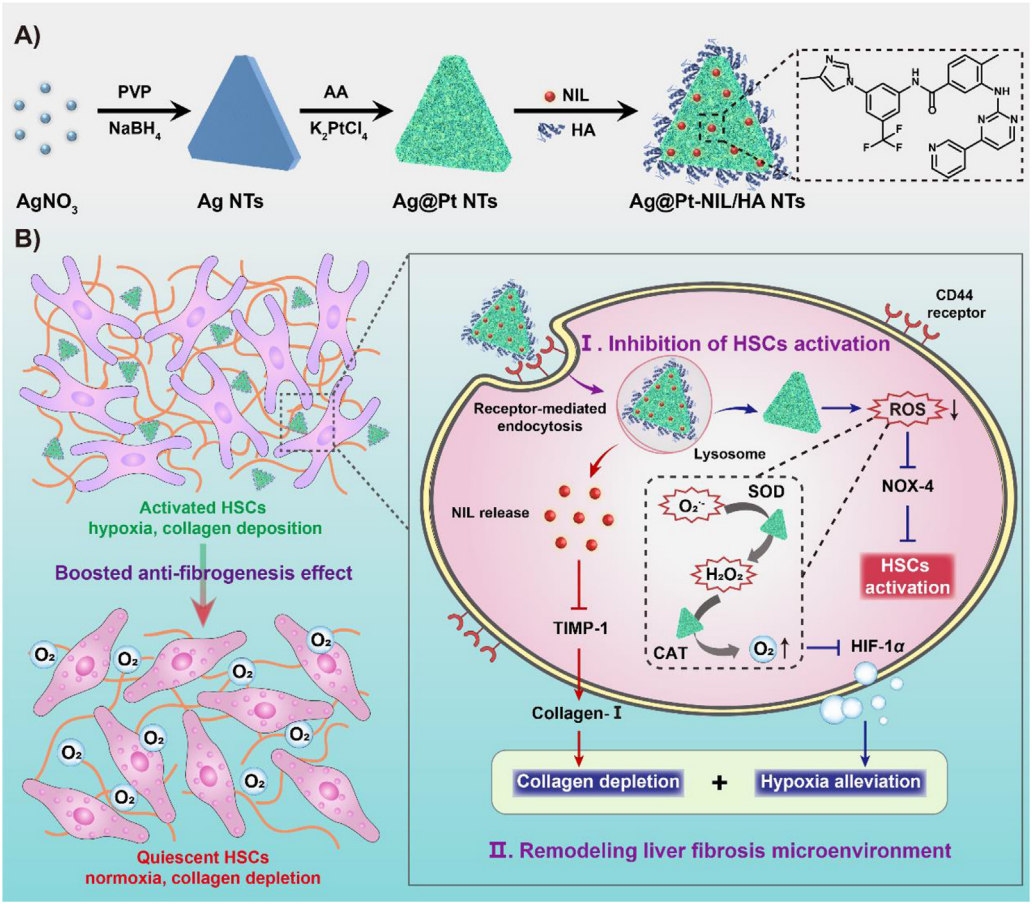

Scheme 1 Schematic drawing of (A) the synthesis and chemical composition of APNH NTs and (B) the mechanisms of their therapeutic activity for the treatment of liver fibrosis. Remodeling of the liver fibrosis microenvironment based on NIL-loaded multicatalytic APNH NTs boosted antifibrogenic activity by simultaneously inhibiting HSCs activation, eliminating ROS, alleviating hypoxia, and depleting collagen.

kit was obtained from Enzo Life Sciences (Farmingdale, NY, USA). DMEM, FBS, and penicillin/streptomycin were obtained from Gibco (Grand Island, NY, USA). 1,1′-Dioctadecyl-3,3,3′,3′-tetramethylindotricarbocyanine iodide (DiR) and 1,1′-dioctadecyl-3,3,3′,3′-tetramethylindocarbocyanine perchlorate (DiL) were purchased from Macklin Reagent Co., Ltd. (Shanghai, China).

Transmission electron microscopy (TEM, Tecnai G2 F20, FEI, Eindhoven, Netherlands) analysis was performed to observe the morphology of Ag and Ag@Pt NTs. High-resolution TEM (HRTEM, Tecnai G2 F20, FEI) and XRPD (D/MAX-2500, Rigaku, Tokyo, Japan) were performed to analyze the crystal structure of Ag@Pt NTs. The X-ray photoelectron spectroscopy (XPS) analysis (AXIS Ultra DLD, Kratos Analytical Ltd., Manchester, UK) was obtained to analyze the elemental valence state of Ag@Pt NTs. Elemental mapping of Ag@Pt NTs was carried out by energy-dispersive X-ray spectroscopy (EDS, Jem-2100f, JEOL, Tokyo, Japan). The absorption analyses were performed using double-beam UV−Vis spectrophotometer UH5300 (Hitachi, Tokyo, Japan). FT-IR spectroscopy was carried out using Tensor 27 (Bruker, Germany) infrared spectrophotometer. Hydrodynamic diameters (HDDs) and zeta potentials were measured on a Malvern Dynamic light scattering (DLS) Zetasizer (Nano ZS, Malvern Instruments, Malvern, UK). Electron spin resonance (ESR) spectra were obtained at ambient temperature using a Bruker EMX ESR spectrometer (Bruker). Confocal microscopy micrographs (CLSM) were captured using Leica SP 8 (Leica, Germany). Flow cytometric analysis was conducted using BD FACS Aria3 (BD, Franklin Lakes, NJ, USA). Western blots were visualized using the ChemiDoc MP System (Bio-Rad, Santa Clara, CA, USA). Fluorescence signals of antibodies-labeled cells and tissues were observed under fluorescence microscope Eclipse Ti−U (Nikon, Tokyo, Japan). *Ex vivo* and *in vivo* fluorescence imaging was performed on an IVIS Spectrum (PerkinElmer, Waltham, MA, USA). Pharmacokinetics and biosafety studies were carried out using inductively coupled plasma mass spectrometer (ICP-MS) Agilent 7900 (Agilent, Santa Clara, CA, USA).

2.2. *Preparation of APNH NTs*

Firstly, the Ag NTs were synthesized according to the previously reported method[30]. Briefly, $AgNO_3$ (50 mmol/L, 200 μL), Na_3CA (75 mmol/L, 2.0 mL), PVP (17.5 mmol/L, 400 μL), H_2O_2 (240 μL) and H_2O (96.16 mL) were added to a flask and stirred for 2 min. After that, $NaBH_4$ (100 mmol/L, 1 mL) was rapidly added to the solution and stirred for another 2 min. After 1 h, Ag NTs were collected by centrifugation (14,800×*g*, 10 min) and washed three times with DI water.

Subsequently, the as-synthesized Ag NTs were dispersed in 10 mL of DI water, followed by the addition of H_2ASc (100 mmol/L, 200 μL) to the solution and vigorous stirring for

30 min. Then, 1 mL of K_2PtCl_4 (15 mmol/L) was added dropwise into the mixture[31]. After constant stirring (2 h), the Ag@Pt NTs were centrifuged (14,800×*g*, 10 min) and washed three times with DI water.

Finally, NIL was loaded onto Ag@Pt NTs through electrostatic interaction. Typically, the obtained Ag@Pt NTs (1 mg/mL, 1 mL) were mixed with NIL solution in DMSO (100 μg/mL, 1 mL) under constant magnetic stirring (6 h). The resulting NIL-loaded Ag@Pt NTs were then dispersed in 2 mL of DI water for further use. After that, HA (1 mg/mL, 1 mL) was dropped into the suspension containing NIL-loaded Ag@Pt NTs and the sample was magnetically stirred. After 24 h, the resulting APNH NTs were dialyzed (MWCO 12 kDa) for 2 days to remove the non-reacted HA. The concentration of APNH NTs was determined in the lyophilized product by weighing.

2.3. Evaluation of SOD-like activity of APNH NTs

The SOD-like activity of APNH NTs was first explored by ESR spectroscopy. The solution containing a spin-trapping reagent BMPO (100 mmol/L), 0.2 mmol/L diethylenetriaminepentaacetic acid, 10 mmol/L xanthine, and 1 U/mL xanthine oxidase was mixed with different concentrations of APNH NTs (50, 100, 200 and 400 μg/mL) and the ESR spectra were recorded after 30 min of ambient incubation. In addition, the inhibition rate of $O_2^{\cdot-}$ was also analyzed using the SOD activity assay kit according to the manufacturer's instructions (Solarbio Science & Technology Co., Ltd.).

2.4. Evaluation of CAT-like activity of APNH NTs

The CAT-like activity of APNH NTs was determined by ESR spectroscopy, quantitation of O_2 generation, and H_2O_2 consumption, respectively. Firstly, different concentrations of APNH NTs (50, 100, 200, and 400 μg/mL) were analyzed by ESR spectroscopy after 30 min incubation. Next, the CAT-like activity was analyzed by measuring O_2 generation. Briefly, the sample containing 10 mmol/L H_2O_2 in PBS was mixed with APNH NTs and the generated O_2 was quantified by a portable dissolved oxygen detector (REX, Shanghai INESA Scientific Instrument Co., Ltd., Shanghai, China) at different times. For the H_2O_2 consumption experiment, 10 mmol/L H_2O_2 and different concentrations of APNH NTs (25, 50, 100, 200, and 400 μg/mL) were mixed, followed by centrifuging the supernatant to determine the absorption of samples at 240 nm. In addition, the inhibition of H_2O_2 by APNH NTs was also detected using the CAT activity assay kit according to the manufacturer's instructions (Solarbio Science & Technology Co., Ltd.).

2.5. Quantification of pH-triggered release of NIL from APNH NTs

In vitro cumulative release kinetics of NIL were analyzed using UV−Vis spectroscopy. Briefly, APNH NTs (1 mg/mL in PBS, 2 mL) were dialyzed (MWCO 1.0 kDa) in PBS (pH 7.4 or 5.0). Within specific pre-defined intervals (1, 2, 4, 6, 8, 10, 12, 24, 48 h), 2 mL of supernatant was sampled and analyzed using UV−Vis spectrophotometry at 260 nm. Afterward, the same volume of PBS was added to the dialysis bag to enable the continuation of analysis without unwanted sample concentration.

2.6. Cell cultures

The LX-2 human HSC line (CL-0560) and LO-2 human normal hepatocytes (HL-7702) were all bought from Life Science &Technology Co., Ltd. (Wuhan, China). LX-2 and LO-2 cells were cultured in DMEM supplemented with 10% (*v*/*v*) FBS and 1% penicillin-streptomycin in a humidified atmosphere containing 5% CO_2 at 37 °C.

2.7. Examination of cytotoxicity of APNH NTs

Briefly, LX-2 and LO-2 cells were seeded in 96-well plates with a density of 1×10^4 cells/well. Next, cells were incubated with different concentrations of APNH NTs (6.25, 12.5, 25, 50 and 100 μg/mL). After further incubation for 24 h, the cells were exchanged to CCK-8 (10 μL) in fresh medium (100 μL) for 1 h at 37 °C and then measured the absorbance at 450 nm. All experiments were conducted in quadruplicate.

2.8. Hemolytic activity of APNH NTs

The hemolytic activity was studied with fresh whole-blood samples of mice. To collect erythrocytes, the blood samples were centrifuged (2467×*g*, 10 min), and gently washed three times. Afterward, 200 μL of diluted erythrocyte suspension was added to 1 mL of APNH NTs dispersion at different concentrations (6.25, 12.5, 25, 50, 100 μg/mL). The samples were incubated for 2 h at 37 °C and then centrifuged (14,800×*g*, 15 min) and quantified by measuring the absorbance at 540 nm. DI Water and PBS were conducted as the positive and negative control, respectively.

2.9. Cellular internalization of APNH NTs

Intracellular localization of APNH NTs was monitored using flow cytometry, CLSM as well as Bio-TEM. For flow cytometry analysis, the LO-2 and LX-2 cells were cultured in 6-well plates at a density of 1×10^6 cells/well. Then, cells were further incubated with 20 μg/mL FITC-labeled APNH NTs for different intervals (2, 4, 6, 8 h), which were washed, centrifuged, and observed by flow cytometry. Additionally, to capture CLSM micrographs, the LX-2 cells were cultured (24 h) in confocal dishes at a density of 1×10^5 cells/dish. After that, cells were incubated with 20 μg/mL FITC-labeled Ag@Pt NTs or APNH NTs. At predefined time intervals, the cells were stained with LysoTracker Red and Hoechst 33342 and observed under CLSM. Similarly, various concentrations of FITC-labeled APNH NTs (1, 2, 4, 10, and 20 μg/mL) for cellular internalization were also investigated. To capture the Bio-TEM micrographs, the LX-2 cells were cultured in 6-well plates at a density of 1×10^6 cells/well. Then, cells were further incubated with 20 μg/mL APNH NTs for 4 h, which were washed, centrifuged, fixed, and observed by TEM.

2.10. Evaluation of the ability of APNH NTs to trigger apoptosis in vitro

LX-2 cells were cultured in 6-well plates at a density of 1×10^6/well. Then, cells were exchanged with the following solutions: fresh medium (control), Ag@Pt NTs (50 μg/mL), NIL (50 μg/mL), APNH NTs (50 μg/mL), APNH NTs (100 μg/mL) and 400 μmol/L H_2O_2 and incubated for another 24 h. Then, the ability of APNH NTs to trigger apoptosis was measured by live/dead cell-staining assay. Besides, the cells were also stained with

Annexin V-FITC apoptosis detection kit and analyzed using flow cytometry.

2.11. *In vitro antioxidative activity of APNH NTs*

The anti-oxidative activity of APNH NTs was analyzed by measuring intracellular total ROS, H_2O_2, and $O_2^{\cdot-}$, respectively. To detect intracellular ROS, LX-2 cells were cultured (24 h) in confocal dishes, and then stimulated with 100 ng/mL LPS, followed by the following treatments: (G1) Control, (G2) Model, (G3) Ag@Pt NTs (50 μg/mL), (G4) NIL (50 μg/mL), (G5) APNH NTs (50 μg/mL) and (G6) APNH NTs (100 μg/mL). Afterward, cells were stained with a DCFH-DA (10 μmol/L) probe for 30 min. In addition, the intracellular H_2O_2 and $O_2^{\cdot-}$ were stained with ROS Green™ H_2O_2 probe (10 μmol/L, 30 min) and DHE probe (10 μmol/L, 30 min), respectively. In all analyses, nuclei were counterstained with Hoechst 33342. Fluorescence signals and fluorescence micrographs were determined by CLSM and flow cytometry, respectively.

2.12. *Western blotting*

Western blotting was employed to analyze the expression of NOX-4, HIF-1α, TIMP-1, α-SMA, and collagen-I either in cell lines or in murine tissues. The primary antibodies were purchased from Boster Biological Technology Co., Ltd. (Pleasanton, CA, USA). The total protein of cells or hepatic tissues were extracted and then measured by Bio-Rad Protein Assay (Bio-Rad). Then, 20 μg of proteins were fractionated by sodium dodecyl sulfate-polyacrylamide gel electrophoresis (SDS-PAGE) electrophoresis and transferred onto poly(vinylidene fluoride) (PVDF) membranes, which were incubated with different primary antibodies and corresponding secondary antibodies and detected using ECL plus kits (Amersham, Piscataway, NJ, USA). Finally, the membranes were visualized by ChemiDoc MP System (Bio-Rad).

2.13. *Cellular hypoxia detection*

The intracellular hypoxia was detected by ROS-ID™ hypoxia/oxidative stress detection kit. The LX-2 cells were pre-seeded into confocal dishes and incubated in the normoxic environment (20 h), followed by subsequent incubation in a hypoxic environment (4 h). After washing with PBS, cells were treated with medium containing Ag@Pt (50 μg/mL), NIL (50 μg/mL), APNH NTs (50 μg/mL) and APNH NTs (100 μg/mL) for 4 h in an atmosphere containing 1% O_2, respectively. Then, cells were stained with hypoxia detection reagent (0.5 mmol/L, 30 min) and nuclei were counterstained with Hoechst 33342 (30 min). After incubation, the cells were observed under CLSM using the excitation wavelength of 405 nm.

2.14. *Cellular immunofluorescence*

LX-2 cells were pre-seeded into the confocal dishes and incubated with Ag@Pt (50 μg/mL), NIL (50 μg/mL), APNH NTs (50 μg/mL) and APNH NTs (100 μg/mL) for 24 h, which were washed and fixed with 4% paraformaldehyde. Then, cells were incubated with 0.5% Triton X-100 and washed three times, blocking the cells (30 min) to eliminate non-specific antibody binding. Later, cells were incubated with anti-α-SMA or anti-collagen-I primary antibodies (Boster Biological Technology Co., Ltd., Pleasanton, CA, USA) at 4 °C in a wet box overnight, washing three times with PBS containing 0.1% Tween and incubating with Cy3-or FITC-conjugated secondary antibody (Beyotime Biotechnology, Jiangsu, China) for 30 min. Finally, the cells were counterstained with mounting agent containing DAPI and observed for fluorescence under a CLSM.

2.15. *Induction of liver fibrosis in mice*

ICR mice (male) were fed at the Laboratory Animal Center of the Chinese Academy of Medical Sciences Institute of Radiology (Tianjin, China) and in compliance with the institution guidelines for maintenance and use of laboratory animals, which were induced by intraperitoneal injections of CCl_4 (2 mL/kg, CCl_4 and olive oil = 1:9, twice a week) for 8 weeks. The normal group was administrated with the same volume of olive oil as the control.

2.16. *Treatment strategy of liver fibrosis in mice*

The ICR mice were treated through the tail vein twice a week with the following samples: (G1) normal group: healthy mice; (G2) model group: fibrotic mice; (G3) 5 mg/kg Ag@Pt NTs in physiological saline; (G4) free NIL (100 μg/mL) dissolved in physiological saline with 2% DMSO and 30% PEG 300 (NIL: 0.2 mg/kg)[32]; (G5) 5 mg/kg APNH NTs in physiological saline; (G6) 10 mg/kg APNH NTs in physiological saline.

2.17. *Tissue biodistribution study*

For the tissue biodistribution studies, DiR-loaded Ag@Pt/HA NTs (instead of NIL-loaded Ag@Pt/HA NTs) were used. For DiR loading, the solution was stirred for 24 h followed by collecting the Ag@Pt-DiR NTs by centrifugation (12,333×*g*, 10 min). Ag@Pt-DiR NTs were then coated with HA according to the previously described protocol. Finally, DiR-loaded Ag@Pt/HA NTs were administrated to normal and fibrotic mice (DiR: 1 mg/kg). At 6 and 12 h, as well as on Days 1, 2, 3, 4, 5, 7, and 9 post-injection, mice were anesthetized using isoflurane and subjected to *in vivo* fluorescence imaging. Besides, on Days 1 and 9, mice were sacrificed to remove livers, hearts, lungs, spleens, and kidneys for *ex vivo* imaging.

2.18. *Evaluation of intrahepatic cell-type-specific distribution and targeting ability*

The cellular localization in the murine liver was further investigated using DiL-loaded NTs (instead of NIL-loaded NTs). The DiL-loaded Ag@Pt NTs or Ag@Pt/HA NTs were administrated to normal and fibrotic mice, respectively. Then, 24 h after the last injection, mice were sacrificed to harvest paraffin-embed liver tissues. The liver tissue was then labeled with anti-albumin (Bioworld Technology, Inc., St. Louis Park, MN, USA) or anti-α-SMA antibody (Boster Biological Technology Co., Ltd.) and incubated at 4 °C overnight, separately. After washing, the tissue was labeled with AlexaFluor 488-labeled secondary antibody (Beyotime Biotechnology). Tissue sections were then counterstained with DAPI and observed under a fluorescence microscope.

2.19. *Evaluation of in vivo anti-fibrogenic activity of APNH NTs*

For analyses, the blood was collected and centrifugated at 4,317×*g* for 10 min. The serum levels of aspartate aminotransferase (AST), alanine aminotransferase (ALT), and alkaline

phosphatase (ALP) were quantified using Animal Blood Routine Tester. Anti-oxidative capacity and collagen quantification were carried out using malondialdehyde (MDA), SOD, ELISA kits, as well as hepatic hydroxyproline (Hyp) assay kits according to the manufacturer's instructions (Jiancheng Biotech).

2.20. Tissue immunofluorescence and histopathology

Immunofluorescence staining of HIF-1α (Boster Biological Technology Co., Ltd.) was conducted on frozen sections and observed using CLSM. Histological staining was performed in paraffin-embedded sections of fibrotic livers and other major organs. The obtained tissues were stained with hematoxylin and eosin (H&E) staining, TUNEL and applied for histopathology analysis.

2.21. High-throughput RNA sequencing

After the treatment, livers from the control (healthy mice), model (fibrotic mice), as well as the APNH NTs-treated groups were collected for RNA extraction and subsequent transcriptomic analysis. The high-throughput sequencing (RNA-Seq) was carried out on a commercial basis by Novogene Co., Ltd. (Beijing, China).

2.22. Pharmacokinetics and biosafety study of APNH NTs

To study the metabolism and excretion of APNH NTs, ICR mice ($n = 3$) were intravenously injected with APNH NTs (5 mg/kg). At different time points post-injection (1, 2, 4, 6, 8, 12, and 24 h), whole blood was collected from the eyeball and dissolved in nitric acid heating at 100 °C. The concentration of Ag and Pt was then quantified by ICP-MS. Furthermore, the urine, feces and major organs were also collected at different time points and analyzed for the pharmacokinetics study.

For the biosafety study, the ICR mice ($n = 3$) were treated with the following samples thrice a week: i) non-treated control, ii) 10.0 mg/kg APNH NTs (high dose), iii) 5.0 mg/kg APNH NTs (medium dose) and iv) 2.0 mg/mL APNH NTs (low dose). After 8-weeks post-treatment, mice were sacrificed to collect blood and major organs (liver, heart, spleen, lungs, and kidneys) for long-term biosafety analysis. The serum biochemical parameters, such as AST, ALT, ALP, albumin (ALB), total protein (TP), blood urea nitrogen (BUN), creatinine (CR) and urea (UA) were quantified using an automated biochemical analyzer.

2.23. Statistical analysis

All data in this study are expressed as mean ± standard deviation (SD). T Student's *t*-test (two-tailed) was used to analyze the difference, in which statistical differences between groups are indicated as NS (no significance), $^{*}P < 0.05$, $^{**}P < 0.01$ and $^{***}P < 0.001$.

3. Results and discussion

3.1. Synthesis and characterization of APNH NTs

In this study, APNH NTs were prepared *via* a three-step reaction as described in detail previously. As shown in Fig. 1A, the TEM micrograph confirmed that the Ag NTs displayed triangular shapes, uniform sizes and homogenous dispersion. From Ag NTs, the Ag@Pt NTs were synthesized through the *in situ* galvanic replacement reaction of K_2PtCl_4 with Ag NTs (Supporting Information Fig. S1). As shown in Fig. 1B and Supporting Information Fig. S2, the Ag@Pt NTs maintained a triangular morphology with a bumpy surface and an average diameter of ~60−70 nm. HRTEM was employed to explore the crystallographic properties of Ag@Pt NTs (Fig. 1C). The lattice spacing was calculated to be 0.256 nm, which corresponds to the crystal surface of (200). In addition, the selected area electron diffraction (SAED) pattern was determined (Fig. 1D), in which (111), (200), (311), and (220) were discovered as the prevalent lattice planes. To further investigate the mechanism of the Ag@Pt NTs alloying process, the EDS mapping was carried out (Fig. 1E and Supporting Information Fig. S3). Ag was found to be distributed homogeneously within the NTs, whereas Pt was mainly dispersed on the surface of Ag. These results confirmed that the synthesis process of Ag@Pt involves the formation of Ag NTs, followed by the galvanic replacement reaction between K_2PtCl_4 and Ag to form the rough surface of the Ag NTs. These findings were further confirmed by XPS and X-ray powder diffraction (XRD) analyses. Specifically, the Ag L-edge and Pt L-edge (Fig. 1F and G) validated that the main Ag species in Ag@Pt NTs were Ag^{+} and Ag^{0} (3d 3/2 and 3d 5/2). In the case of Pt, the main valence states were Pt^{2+} and Pt^{0} (4f 5/2 and 4f 7/2). Additionally, the XRD pattern (Fig. 1H) of the Ag@Pt NTs demonstrated (111), (200), (311), and (220) characteristic diffraction peaks, which is consistent with the SAED results.

After the synthesis of Ag@Pt NTs, NIL was loaded onto the structure through electrostatic interactions (Fig. 1I). The loading capacity (LC) and loading efficiency (LE) of NIL in NPs were determined to evaluate their drug loading property by the UV−Vis spectroscopy (Supporting Information Figs. S4−S6). At the concentration of 50 μg/mL, the LC and LE were 4.12% and 41.2%, respectively. Subsequently, Ag@Pt-NIL NTs were coated using HA and then purified. As demonstrated in the Fourier transform infrared (FT−IR) spectra in Supporting Information Fig. S7, the resulting APNH NTs exhibited C−H stretching at 2800 cm^{-1}, which is characteristic of HA. Furthermore, we determined the HDDs of the Ag NTs, Ag@Pt NTs and APNH NTs (Supporting Information Fig. S8). The average HDD of the APNH NTs (~140 nm) was slightly larger than that of the Ag NTs and Ag@Pt NTs. The successful synthesis of APNH NTs was finally confirmed by zeta potential analysis, demonstrating a zeta potential evolution during the synthesis (Supporting Information Fig. S9).

3.2. ROS scavenging activity of Ag@Pt NTs

To further explore the enzymomimetic activity of Ag@Pt NTs, $O_2^{\cdot-}$ and H_2O_2, as two major representatives of ROS, were employed to investigate the ROS elimination capacity of Ag@Pt NTs. To evaluate the SOD-like activity (schematized in Fig. 2A), the efficiency of $O_2^{\cdot-}$ scavenging was evaluated by electron ESR spectroscopy using BMPO. As shown in Fig. 2B and Supporting Information Fig. S10, $O_2^{\cdot-}$ was consumed gradually in a concentration and time-dependent manner. To confirm this phenomenon, the inhibition rate of $O_2^{\cdot-}$ was further quantified with a SOD activity assay kit. As shown in Fig. 2C, the inhibition rate of $O_2^{\cdot-}$ by Ag@Pt NTs (200 μg/mL) was calculated to be 15.3%, which validates that Ag@Pt NTs exhibit exceptional enzymomimetic properties and are useful as nanozymes for $O_2^{\cdot-}$ elimination.

After confirming the SOD-like activity, we evaluated the CAT-like activity of Ag@Pt NTs (schematized in Fig. 2D). Similar to

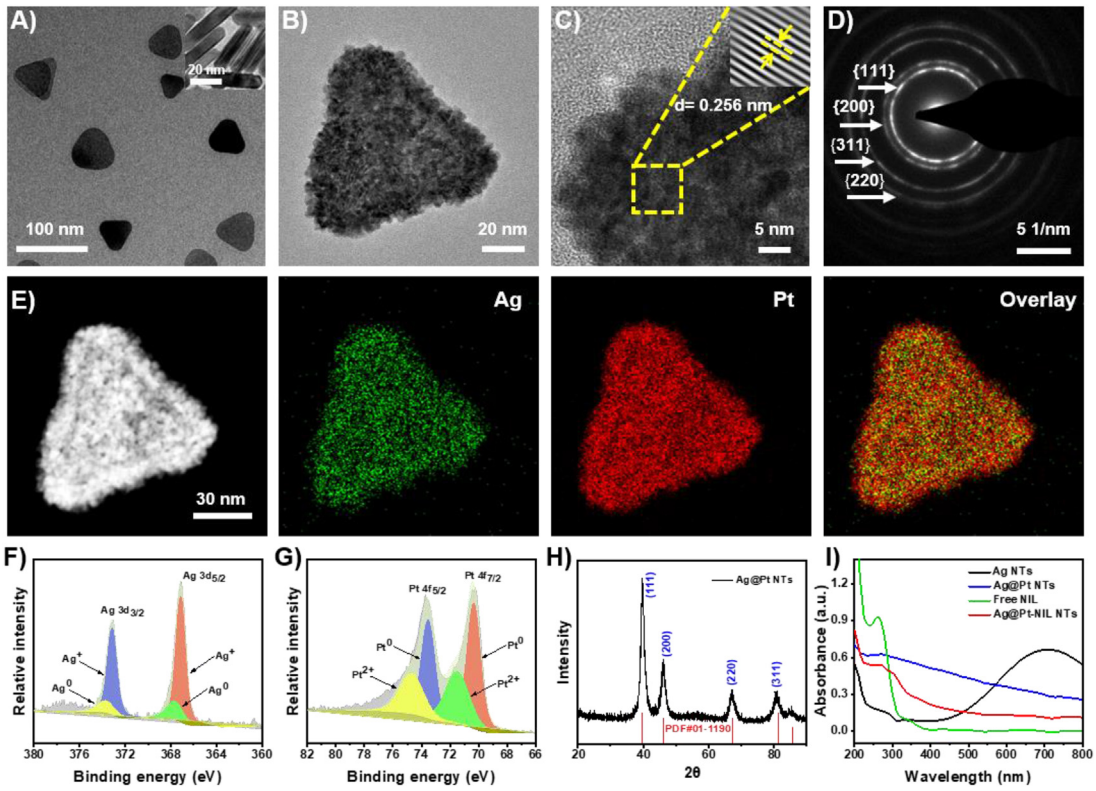

Figure 1 Physicochemical characterization of APNH NTs. (A) Representative TEM micrograph of Ag NTs. (B) Representative TEM micrograph of Ag@Pt NTs. (C) Representative HRTEM micrograph of Ag@Pt NTs. The inset is the inverse fast Fourier transformation image of the area demarcated by the yellow dashed line. (D) SAED patterns of Ag@Pt NTs. (E) EDS mapping of Ag@Pt NTs. Green represents Ag, and red represents Pt in the Ag@Pt NTs. (F) (G) XPS survey of Ag 3d 3/2 and 5/2 and Pt 4f 5/2 and 7/2. (H) XRPD pattern of Ag@Pt NTs. (I) UV−Vis spectra of Ag NTs, Ag@Pt NTs, free NIL and Ag@Pt-NIL.

$O_2^{\cdot-}$, ESR analysis revealed that H_2O_2 was consumed gradually in a concentration and time-dependent manner (Fig. 2E and Supporting Information Fig. S11). Additionally, the inhibition rates of H_2O_2 by Ag@Pt were examined with a CAT activity assay kit, which confirmed the efficient H_2O_2 degradation by Ag@Pt NTs (Fig. 2F). Furthermore, we found that due to the CAT-like activity of Ag@Pt NTs, catalytic decomposition of H_2O_2 efficiently generated O_2 (Fig. 2G). As shown in Fig. 2H and Supporting Information Fig. S12, O_2 generation by Ag@Pt NTs occurred in a concentration and time-dependent manner. Finally, we aimed to examine the release kinetics of NIL from APNH NTs. For this purpose, we incubated the APNH NTs in solutions mimicking neutral conditions (pH 7.4) and the acidic environment of the endolysosomal compartment (pH 5.0). By examining the characteristic absorption maxima of NIL (260 nm), the cumulative release of NIL was quantified from the NIL standard calibration curve. As shown in Fig. 2I, after 48 h, up to 81.9 ± 1.78% of NIL was released after incubation in acidic conditions, while only 16.7 ± 1.21% of NIL was released at pH 7.4. These data indicate the pH-triggerable NIL release properties of APNH NTs and NIL-loading stability in the pH of blood circulation.

3.3. *Cellular internalization and cytotoxicity of APNH NTs In vitro*

Inspired by the physicochemical properties of APNH NTs, we further continued with an *in vitro* investigation of the biological properties of APNH NTs. First, we investigated the potential cytotoxicity of APNH NTs in LX-2 and LO-2 cells. In LX-2 cells, 100 μg/mL APNH NTs caused a ∼25% decline in viability. In contrast to LX-2 cells, in LO-2 cells, the highest applied concentration of APNH NTs caused only a ∼13% decline in viability, indicating good biocompatibility (Fig. 3A). In addition, APNH NTs (100 μg/mL) induced negligible (<2.0%) hemolysis in murine erythrocytes (Fig. 3B), indicating the great hemocompatibility of APNH NTs. For cellular internalization, we initially verified the cellular uptake of Ag@Pt and APNH NTs in LX-2 cells. The Pearson's correlation coefficient representing the colocalization of FITC fluorescence and LysoTracker were determined to be 0.52 and 0.68, respectively, suggesting that the HA increased the internalization of LX-2 cells (Supporting Information Fig. S13). Next, the cell internalization of APNH NTs was studied in LO-2 and LX-2 cells *via* flow cytometry analysis (Supporting Information Figs. S14−S16), which revealed APNH NTs were more efficient internalization in LX-2 cells than LO-2 cells in the same interval. Ample evidence suggests that the endocytosis of NPs is strictly associated with the endolysosomal compartments[26]. Therefore, we then investigated the kinetics of the cellular uptake of APNH NTs by LX-2 cells and the possible post-endocytosis storage of APNH NTs in lysosomes. As shown in Fig. 3C, the obtained data revealed time-dependent uptake of APNH NTs, indicating efficient internalization by LX-2 cells. The intracellular FITC signal intensity was positively correlated with the applied dose of APNH NTs (Supporting Information Fig. S17). It is worth noting that CLSM analyses revealed partial colocalization of APNH NTs with LysoTracker Red-stained endolysosomes. Thus, the intracellular fate was

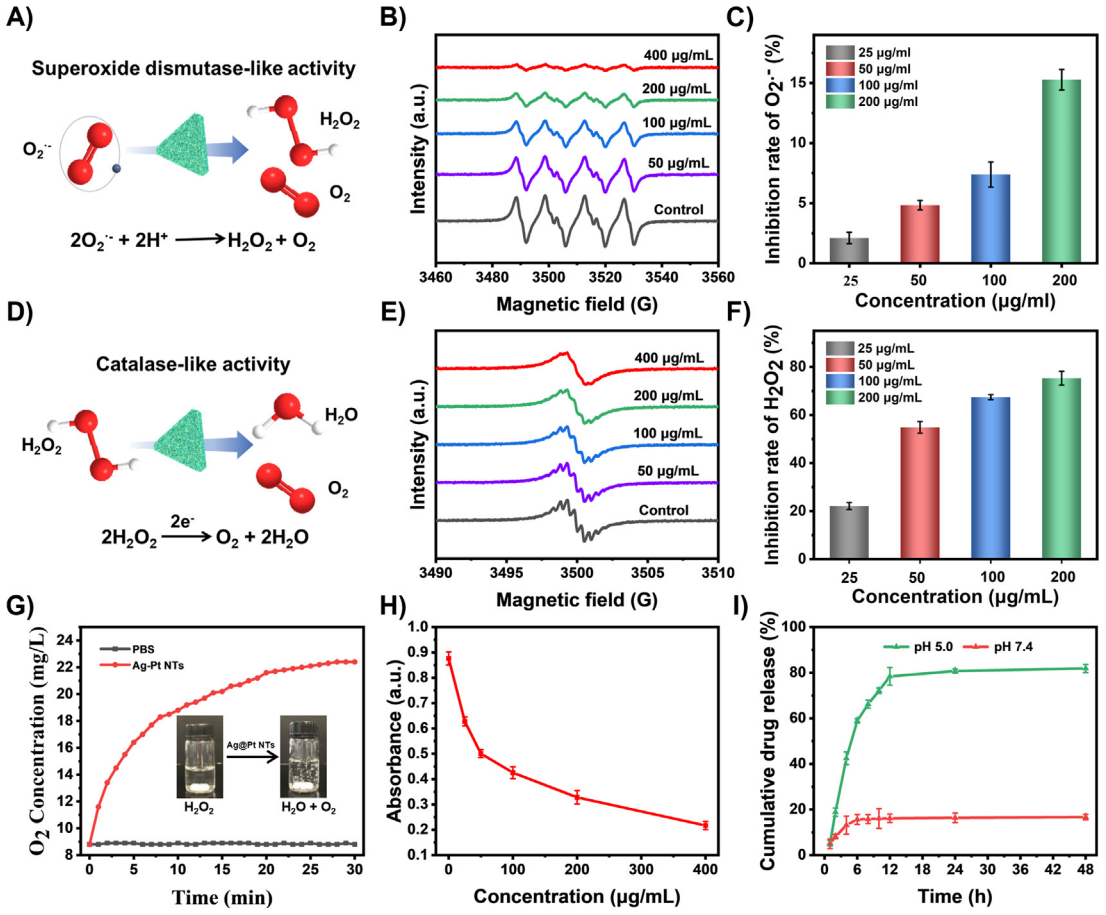

Figure 2 ROS scavenging activities of APNH NTs and evaluation of the cumulative release kinetics of NIL. (A) Schematic presentation of the SOD-like activity of Ag@Pt NTs. (B) ESR spectra demonstrating $O_2^{\cdot-}$ scavenging with different concentrations of Ag@Pt NTs. (C) $O_2^{\cdot-}$ inhibition rates caused by treatment with different concentrations of Ag@Pt NTs quantified with a SOD activity assay kit. Data are shown as the mean ± SD (n = 3). (D) Schematic presentation of the CAT-like activity of Ag@Pt NTs. (E) ESR spectra demonstrating H_2O_2 scavenging with different concentrations of Ag@Pt NTs. (F) H_2O_2 inhibition rates caused by treatment with different concentrations of Ag@Pt NTs validated with a CAT activity assay kit. Data are shown as the mean ± SD (n = 3). (G) O_2 generation upon mixing Ag@Pt NTs (50 μg/mL) and H_2O_2 (10 mmol/L) in PBS. (H) The concentration-dependent CAT-like activity of Ag@Pt NTs verified by H_2O_2 elimination. (I) Cumulative *in vitro* release of NIL from APNH NTs in environments with different pH values (pH 5.0 and 7.4).

investigated by bio-TEM (Supporting Information Fig. S18), which revealed that APNH NTs were endocytosed by LX-2 cells and were observed either on the cell membrane or as aggregates in endolysosomes. Importantly, bio-TEM also showed the presence of APNH NTs in the cytoplasm of LX-2 cells, indicating their ability to perform endosomal escape.

Furthermore, the ability of APNH NTs to trigger apoptosis was investigated by fluorescence microscopy as well as flow cytometry. Using Calcein-AM/PI apoptosis kit, the dead cells and living cells were stained by red and green fluorescence, respectively. After APNH NTs treatment, the red fluorescent in LX-2 cells was markedly increased, indicating that APNH NTs are able to trigger some amount of apoptosis in LX-2 cells (Fig. 3D). As shown in Fig. 3E, APNH NTs could substantially increase the population of dead cells (11.8%) and lessen the number of living cells (89.2%) than control group (1.1% and 98.9%). Taken together, the obtained data confirmed that APNH NTs can induce apoptosis and thus inhibit cell proliferation.

3.4. *APNH NTs effectively alleviate liver fibrosis in vitro*

Liver fibrosis is frequently associated with excessive ROS production that overwhelms the endogenous antioxidant capacity[33]. During liver fibrogenesis, ROS serve as signaling mediators and activate HSCs to synthesize abundant collagen[34]. Thus, the elimination of ROS to avoid HSCs activation may be a powerful approach for liver fibrosis therapy[35,36]. Notably, NOX enzymatic complexes are the primary sources of endogenous ROS formation[37]. Among them, NOX-4, a nonphagocytic NOX homolog that can generate ROS and activate HSCs, has been proven to play an important role in liver fibrosis development (schematized in Fig. 4A)[38,39]. In this study, the effect of APNH NTs on oxidative stress in LPS-activated LX-2 cells were evaluated by flow cytometry (Fig. 4B). APNH NTs significantly decreased the intracellular ROS levels (from 73.8% to 34.5%). Using CLSM, we further investigated the intracellular amounts of total ROS, H_2O_2 and $O_2^{\cdot-}$. As shown in Fig. 4C, LPS stimulation markedly

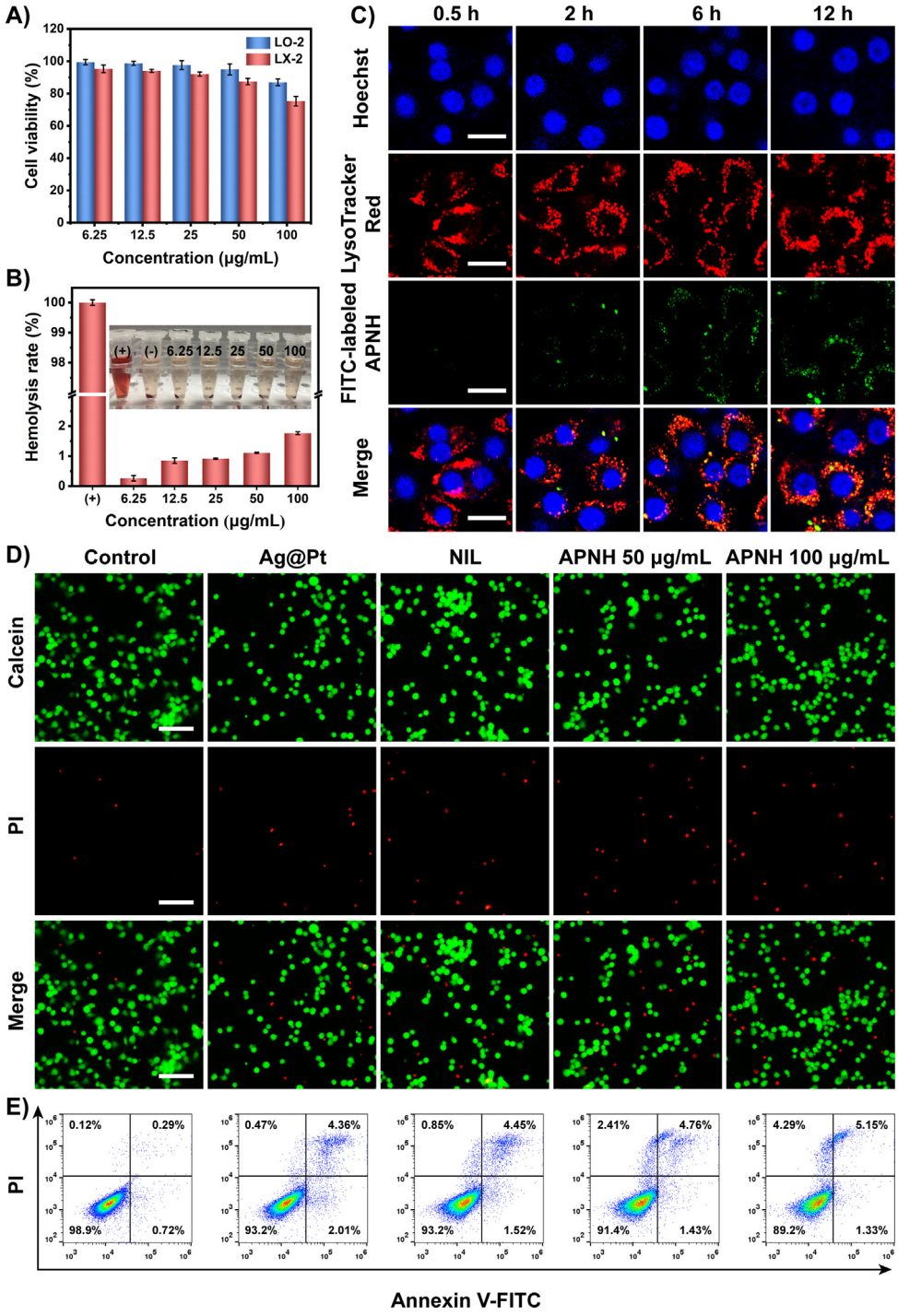

Figure 3 Cellular internalization and *in vitro* cytotoxicity of APNH NTs. (A) Viability of LO-2 and LX-2 cells treated with different concentrations of APNH NTs for 24 h. (B) Hemolytic activity of APNH NTs in murine erythrocytes. (C) CLSM micrographs showing the kinetics of the cellular uptake of FITC-labeled APNH NTs by LX-2 cells and their intracellular fate in different time intervals (0.5, 2, 6, 12 h). Scale bar, 20 μm. (D) Fluorescence micrographs of LX-2 cells after different treatments for 24 h co-stained with Calcein AM/PI. Green (calcein AM), live cells; red (PI), dead cells. Scale bar, 100 μm. (E) Flow cytometry analysis of apoptosis induction in LX-2 cells after exposure to the noted treatments for 24 h. Data are shown as the mean ± SD ($n = 3$). NS (no significance), $^{*}P < 0.05$, $^{**}P < 0.01$, $^{***}P < 0.001$.

enhanced the total ROS levels in LX-2 cells. This phenomenon was further inhibited after Ag@Pt NTs and APNH NTs administration. Interestingly, LX-2 cells treated with free NIL also showed a slight decrease in ROS levels, indicating a synergistic antioxidant effect of Ag@Pt NTs with NIL. After confirming the ROS scavenging ability of APNH NTs, we further decided to delineate the possible scavenging activity toward H_2O_2 and $O_2^{\cdot-}$. In line with the total amount of ROS, the H_2O_2 and $O_2^{\cdot-}$ fluorescence signals were attenuated due to APNH NTs treatment. The above findings were further confirmed by quantitation of the

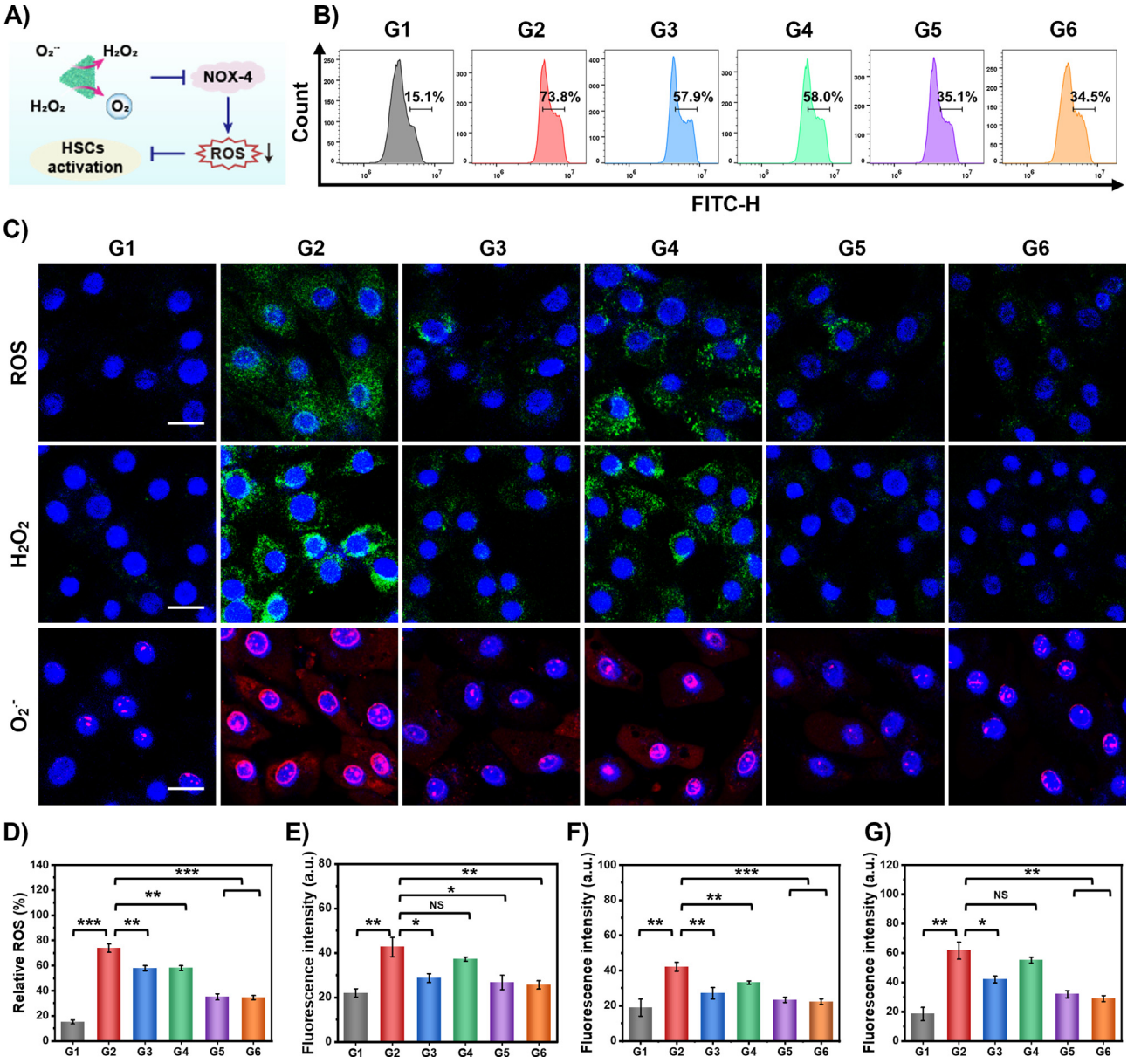

Figure 4 *In vitro* antioxidative and antifibrogenic activities of APNH NTs to inhibit HSCs activation. (A) Schematic depiction of the antifibrogenic mechanism of APNH NTs scavenging NOX-4-generated ROS. (B) Flow cytometry analysis of ROS scavenging in LX-2 cells after different treatments for 24 h analyzed by DCFH-DA staining. (C) CLSM micrographs of total intracellular ROS, H_2O_2 and $O_2^{\cdot-}$ in LX-2 cells exposed to the noted treatments for 24 h. Scale bar, 20 μm. (D) Quantitation of total ROS levels in LX-2 cells. Semiquantitative evaluation of CLSM micrographs showing (E) total ROS, (F) H_2O_2 and (G) $O_2^{\cdot-}$. G1: control, G2: model (LPS), G3: LPS + Ag@Pt NTs (50 μg/mL), G4: LPS + NIL (50 μg/mL), G5: LPS + APNH NTs (50 μg/mL), and G6: LPS + APNH NTs (100 μg/mL). Data are shown as the mean ± SD ($n = 3$). NS (no significance), $^*P < 0.05$, $^{**}P < 0.01$, $^{***}P < 0.001$.

flow cytometry and fluorescence micrographs (Fig. 4D−G). Taken together, the obtained results confirmed that APNH NTs protect LX-2 cells by eliminating intracellular ROS.

Compelling evidence has revealed that HIF-1α is the hallmark of the hypoxic microenvironment, while collagen-I is the predominant ECM component during the development of liver fibrosis[40]. Thus, remodeling of the microenvironment of liver fibrosis through hypoxia alleviation and collagen depletion could produce an antifibrogenic effect (schematized in Fig. 5A). To investigate this phenomenon, we first examined HIF-1α expression in LX-2 cells cultured in a hypoxic environment (Fig. 5B and Supporting Information Fig. S19). The obtained results revealed that APNH NTs treatment significantly decreased HIF-1α expression in LX-2 cells. In addition, it was found that the expression levels of NOX-4, TIMP-1, collagen-I and α-SMA were substantially decreased after APNH NTs exposure (Fig. 5C and Supporting Information Fig. S20). These data underpin the hypothesized mechanism of the antifibrogenic activity of APNH NTs.

Subsequently, intracellular oxygen levels in LX-2 cells were explored to further confirm that APNH NTs alleviate the hypoxic microenvironment. As shown in Fig. 5D, APNH NTs caused a significant decrease in the hypoxic environment, which is likely due to the O_2 generated from the H_2O_2 catalytic decomposition by APNH NTs. Moreover, immunofluorescence visualization of

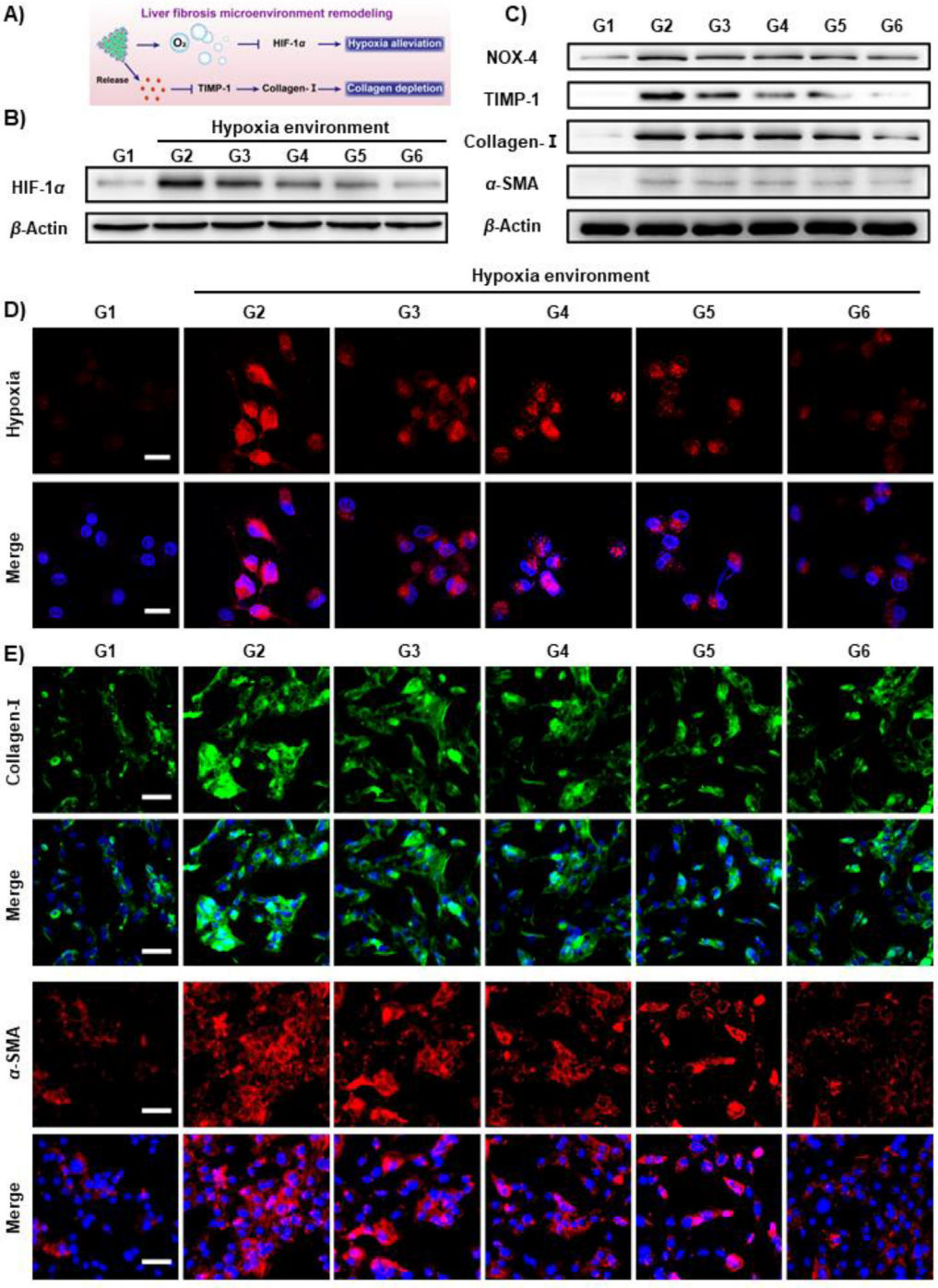

Figure 5 *In vitro* activity of APNH NTs to alleviate hypoxia and deplete collagen. (A) Schematic depiction of the antifibrogenic activity of APNH NTs through hypoxia alleviation and collagen depletion. (B) The expression of HIF-1α in LX-2 cells cultured in a hypoxic environment and exposed to the noted treatments for 24 h. G1: control (normoxia), G2: model (hypoxia), G3: hypoxia + Ag@Pt NTs (50 μg/mL), G4: hypoxia + NIL (50 μg/mL), G5: hypoxia + APNH NTs (50 μg/mL), and G6: hypoxia + APNH NTs (100 μg/mL). (C) The expression of NOX-4, TIMP-1, collagen-I and α-SMA in LX-2 cells exposed to the noted treatments for 24 h. G1: control (normal), G2: model (LPS), G3: LPS + Ag@Pt NTs (50 μg/mL), G4: LPS + NIL (50 μg/mL), G5: LPS + APNH NTs (50 μg/mL), and G6: LPS + APNH NTs (100 μg/mL). (D) CLSM micrographs of the intracellular hypoxia levels in LX-2 cells cultured under normoxic or hypoxic conditions and treated with the noted treatments for 24 h. Scale bar, 25 μm. (E) The expression of α-SMA and collagen-I examined by immunofluorescence after different treatments for 24 h. Scale bar, 50 μm. Data are shown as the mean ± SD ($n = 3$). NS (no significance), $^{*}P < 0.05$, $^{**}P < 0.01$, $^{***}P < 0.001$.

collagen-I and α-SMA in LX-2 cells implied that APNH NTs trigger the antifibrogenic effect *in vitro* (Fig. 5E).

3.5. Biodistribution and targeting ability of APNH NTs in vivo

For the biodistribution study, we intraperitoneally injected ICR mice with saline or CCl_4 twice a week for a total of 8 weeks[41]. Then, the mice were intravenously injected with the DiR or DiL-loaded Ag@Pt/HA NTs. DiR or DiL were loaded on the surface of Ag@Pt NTs mainly owing to hydrophobic interaction and electrostatic interaction, which was confirmed by DLS analysis showing no significant effects of labeling on HDD of Ag@Pt NTs, while shifting the zeta potential to slightly positive value (to 3.98 mV from −21.10 mV) (Supporting Information Figs. S21 and S22).

The LC of DiR was determined by UV−Vis spectroscopy, which was calculated at nearly 2.75% (Fig. S22 and Supporting Information Fig. S23). After treatment, *in vivo* fluorescence imaging was performed to explore the biodistribution in the normal and fibrotic groups, respectively (schematized in Fig. 6A). As shown in Fig. 6B, the DiR-loaded Ag@Pt/HA NTs displayed significant hepatic bioaccumulation in both normal and fibrotic mice 6 h post-intravenous administration. This was plausibly due to the entrapment of DiR-loaded Ag@Pt/HA NTs by the hepatic reticuloendothelial system[19,42]. In both experimental groups, the most intense hepatic fluorescence was observed 12 h post-administration, indicating the time point of the highest bioaccumulation of DiR-loaded Ag@Pt/HA NTs. Interestingly, in normal group, DiR-loaded Ag@Pt/HA NTs exhibited a rapid decline in signal intensity, which may be due to the normal hepatic clearance capacity. In contrast, the fluorescence intensity in the fibrotic group was maintained for a longer period of time and observable until experimental termination (Day 9), which is likely a result of the dysfunction of the liver and collagen accumulation due to induced fibrosis[32].

On Days 1 and 9, the livers, hearts, spleens, lungs and kidneys were utilized to measure the *ex vivo* fluorescence emission of bioaccumulated DiR-loaded Ag@Pt/HA NTs (Fig. 6C). The results revealed that the fluorescence of DiR-loaded Ag@Pt/HA NTs in the livers of normal and fibrotic mice was much higher than that in other tissues, confirming successful liver bioaccumulation. In addition, the fluorescence intensities in the fibrotic group were stronger than those observed in normal mouse livers, which further demonstrated the enhanced bioaccumulation of DiR-loaded Ag@Pt/HA NTs in fibrotic liver tissues. The results of total fluorescence intensity in different times or organs were consistent with the above explanation (Fig. 6D and E).

Besides, the targeting ability and cell-specific distribution of APNH NTs in liver tissues were investigated *via* fluorescence imaging of hepatocytes (albumin-positive) and HSCs (α-SMA-positive). To test the HSCs-targeting ability, instead of NIL, Ag@Pt/HA NTs were loaded with DiL to form DiL-loaded Ag@Pt/HA NTs, enabling facile fluorescence visualization of the biodistribution. As shown in Fig. 6F, the normal liver sections demonstrated only weak DiL fluorescence, indicating the negligible uptake of DiL-loaded Ag@Pt/HA NTs. In contrast, fibrotic liver sections displayed strong DiL signals observable in both hepatocytes and HSCs. Furthermore, the DiL-loaded Ag@Pt NTs (without HA coating) were also conducted in fibrotic mice in a similar manner. Compared to Ag@Pt NTs, the DiL red signal of the APNT NTs was found to extensively merge with the green signal of stained HSCs, showing as the yellow signal (Supporting Information Fig. S24). This finding indicated that the majority of the DiL-loaded Ag@Pt/HA NTs were bioaccumulated in the activated HSCs and confirmed the superb targeting efficiency of APNH NTs due to surface decoration with HA.

3.6. APNH NTs effectively alleviate liver fibrosis in vivo

After confirming the exceptional targeting properties of APNH NTs, we further assessed their antifibrogenic activity *in vivo*. For this purpose, different formulations were administered to mice twice a week for a total of 4 weeks (5−8 W), and the therapeutic effect of different formulations was evaluated after the last dose (schematized in Fig. 7A). Importantly, as shown in Fig. 7B, extensive overexpression of HIF-1α was observed in the untreated CCl_4-induced group. Notably, APNH NTs treatment resulted in a significant reduction in HIF-1α expression, suggesting successful alleviation of the hypoxic microenvironment. In addition, we analyzed the hepatoprotective activity of APNH NTs by staining apoptotic liver cells. The fibrotic mice receiving APNH NTs exhibited the lowest levels of apoptotic cells compared to the NIL alone or Ag@Pt NTs treatment groups (Fig. 7C and Supporting Information Fig. S25), confirming the APNH NTs-mediated protection of liver cells against the cytotoxic effects of liver fibrosis. Moreover, as shown in Fig. 7D, tissue hyperplasia, inflammatory cell infiltration and cellular steatosis were detected in the untreated fibrotic group. Interestingly, these histological features were markedly alleviated in the APNH NTs-treated cohorts. Further quantitation of AST (Supporting Information Fig. S26) and ALT (Supporting Information Fig. S27) confirmed that APNH NTs administration resulted in the restoration of hepatic functions. These findings indicated that ROS clearance by APNH NTs may likely contribute to a reduction in oxidative stress, enhancing the hepatoprotective effects of APNH NTs. Based on APNH NTs-induced HSCs activation and their ability to remodel the microenvironment of liver fibrosis *in vitro*, the antifibrogenic activity of APNH NTs was further explored by analyzing liver collagen deposition by Sirius Red staining (Fig. 7E and Supporting Information Fig. S28), Masson's trichrome staining (Fig. 7F), as well as immunostaining for α-SMA (Fig. 7G) and collagen-I (Fig. 7H). Compared to the NIL alone or Ag@Pt NTs treatment groups, the obtained results convincingly confirmed the ability of the APNH NTs to effectively reduce collage accumulation. The phenomenon of APNH NTs-mediated reduction in collagen accumulation was reconfirmed by quantifying total Hyp (Supporting Information Fig. S29). Importantly, the ability of APNH NTs to alleviate liver fibrosis *in vivo* was further evidenced by examining the concentration of MDA (Supporting Information Fig. S30) and SOD activity (Supporting Information Fig. S31), which were consistent with the previous ROS-reacting activity results of APNH NTs *in vitro*. Investigation of the secretion of hepatic inflammatory cytokines (IL-1β, IL-6, and TNF-α) revealed the weakest hepatic inflammation in the APNH NTs-treated cohorts (Supporting Information Fig. S32). In addition, the analysis of these inflammatory factors in murine serum shown in Supporting Information Fig. S33 was in line with the levels observed in the liver. Finally, the analysis of serum ALP, ALB, TP, BUN and CR (Supporting Information Figs. S34 and S35) and histopathological examination of H&E-stained sections of the heart, spleen, lung and kidney (Supporting Information Fig. S36) revealed that there was no significant undesired organ damage caused by APNH NTs, which validates their great biocompatibility.

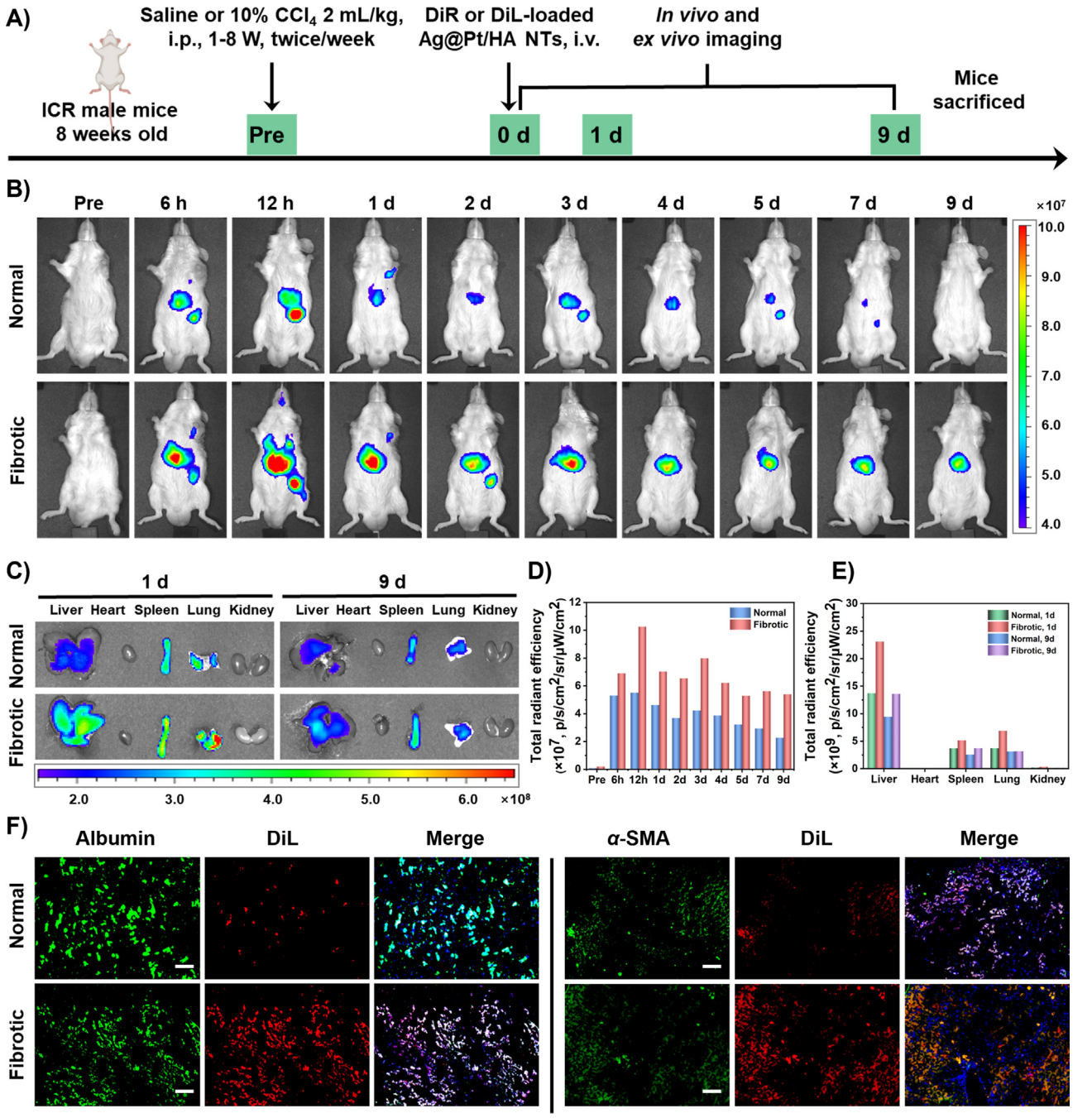

Figure 6 *In vivo* distribution and targeting ability studies of DiR or DiL-loaded Ag@Pt/HA NTs. (A) Schematic diagram showing the induction of liver fibrosis and administration DiR or DiL-labeled Ag@Pt/HA NTs in mice. (B) Representative *in vivo* near-infrared fluorescent photographs of normal and fibrotic mice treated with DiR-loaded Ag@Pt/HA NTs. (C) *Ex vivo* fluorescence imaging of extracted tissues. Fluorescence intensities in (D) the liver and (E) other major organs extracted at the experimental endpoint expressed as total radiant efficiency. (F) Intrahepatic cell type-specific biodistribution of DiL-labeled Ag@Pt/HA NTs in normal and CCl_4-induced mice. Liver tissues were sectioned and immunostained with anti-albumin antibody (green) or anti-α-SMA antibody (green) for hepatocytes or activated HSCs, respectively. Nuclei were counterstained with DAPI (blue). The fluorescence of DiL is shown in red. Scale bar, 100 μm. Data are shown as the mean ± SD ($n = 3$).

3.7. In vivo molecular mechanisms of APNH NTs therapeutic activity

To further analyze the molecular mechanisms responsible for APNH NTs therapeutic activity, we performed a comparative RNA-Seq analysis of the liver transcriptome of control (healthy mice), model (fibrotic mice) and APNH NTs-treated mice. The total gene expression patterns of these cohorts are shown in Venn diagrams in Fig. 8A and Supporting Information Fig. S37, volcano plots in Fig. 8B and Supporting Information Fig. S38, and heatmaps with hierarchical clustering dendrograms (Fig. 8C, Supporting Information Figs. S39 and S40). Analysis of the

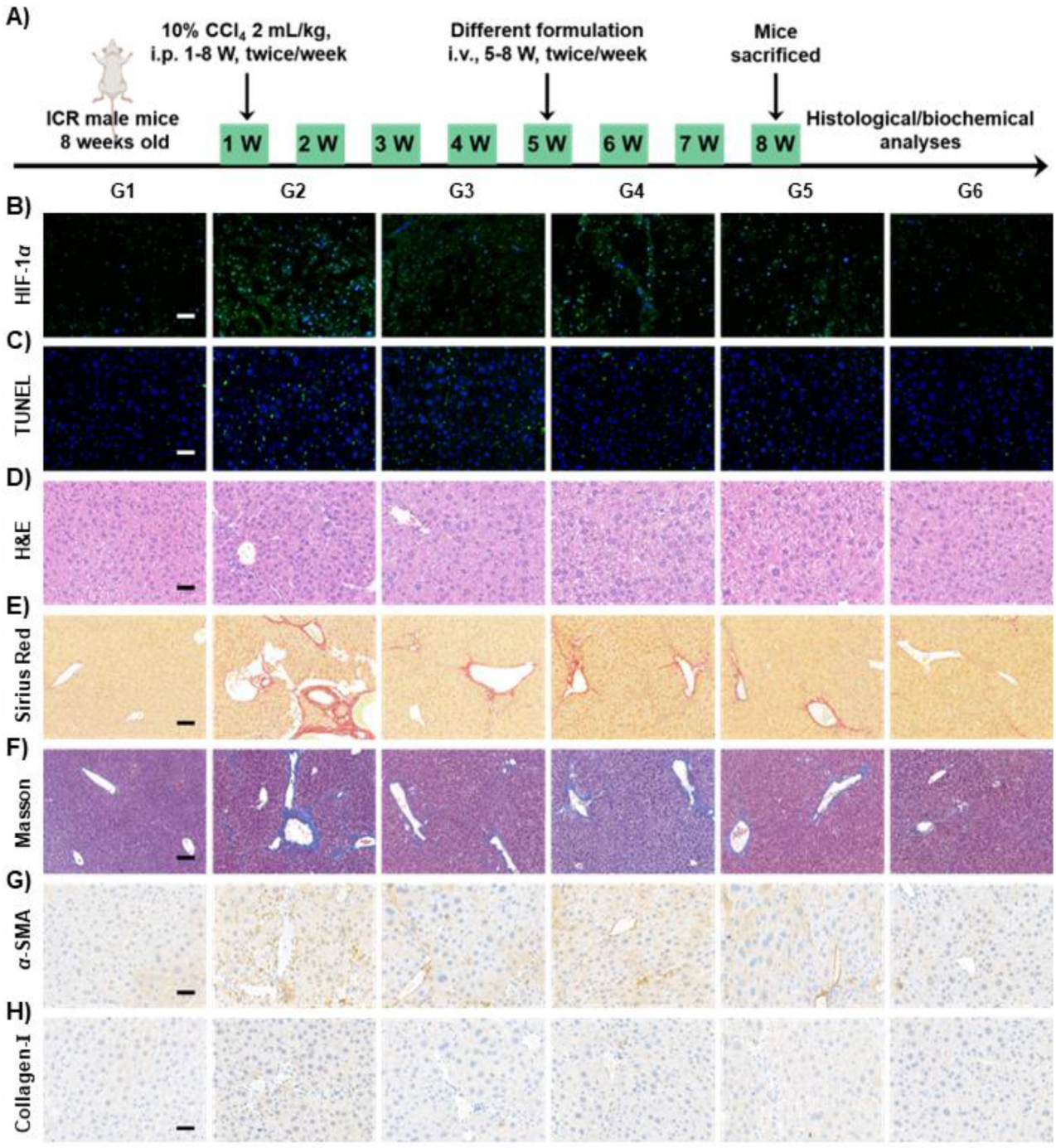

Figure 7 *In vivo* antifibrogenic activity of APNH NTs. (A) Schematic diagram showing the induction of hepatic fibrosis by CCl_4 in mice and the administration with different formulations for therapy. (B) Immunofluorescence of HIF-1α in liver tissue sections. Nuclei were counterstained with DAPI. (C) Apoptotic cells in the liver tissue sections stained using a TUNEL assay. (D) Representative H&E-stained liver tissue sections. Micrographs showing hepatic collagen content visualized using (E) Sirius Red and (F) Masson's trichrome staining. Immunohistochemical staining of (G) α-SMA and (H) collagen-I. Scale bars, 100 μm. G1: control (healthy mice), G2: model (fibrotic mice), G3: Ag@Pt NTs (5 mg/kg), G4: NIL (0.2 mg/kg), G5: APNH NTs (5 mg/kg), and G6: APNH NTs (10 mg/kg). Data are shown as the mean ± SD ($n = 3$). NS (no significance), $^{*}P < 0.05$, $^{**}P < 0.01$, $^{***}P < 0.001$.

differentially expressed genes (DEGs) revealed pronounced differential expression patterns among the tested cohorts. In particular, it was identified that while 11,633 genes were found to be co-expressed in the model and APNH NTs cohorts, 471 DEGs were exclusively expressed in APNH NTs-treated mice. In addition, 398 and 557 commonly expressed genes were significantly up or downregulated, respectively, which clearly confirms the gene expression relationship between the model and APNH NTs-treated groups. Furthermore, unguided principal component analysis (PCA) of the detected DEGs confirmed substantially

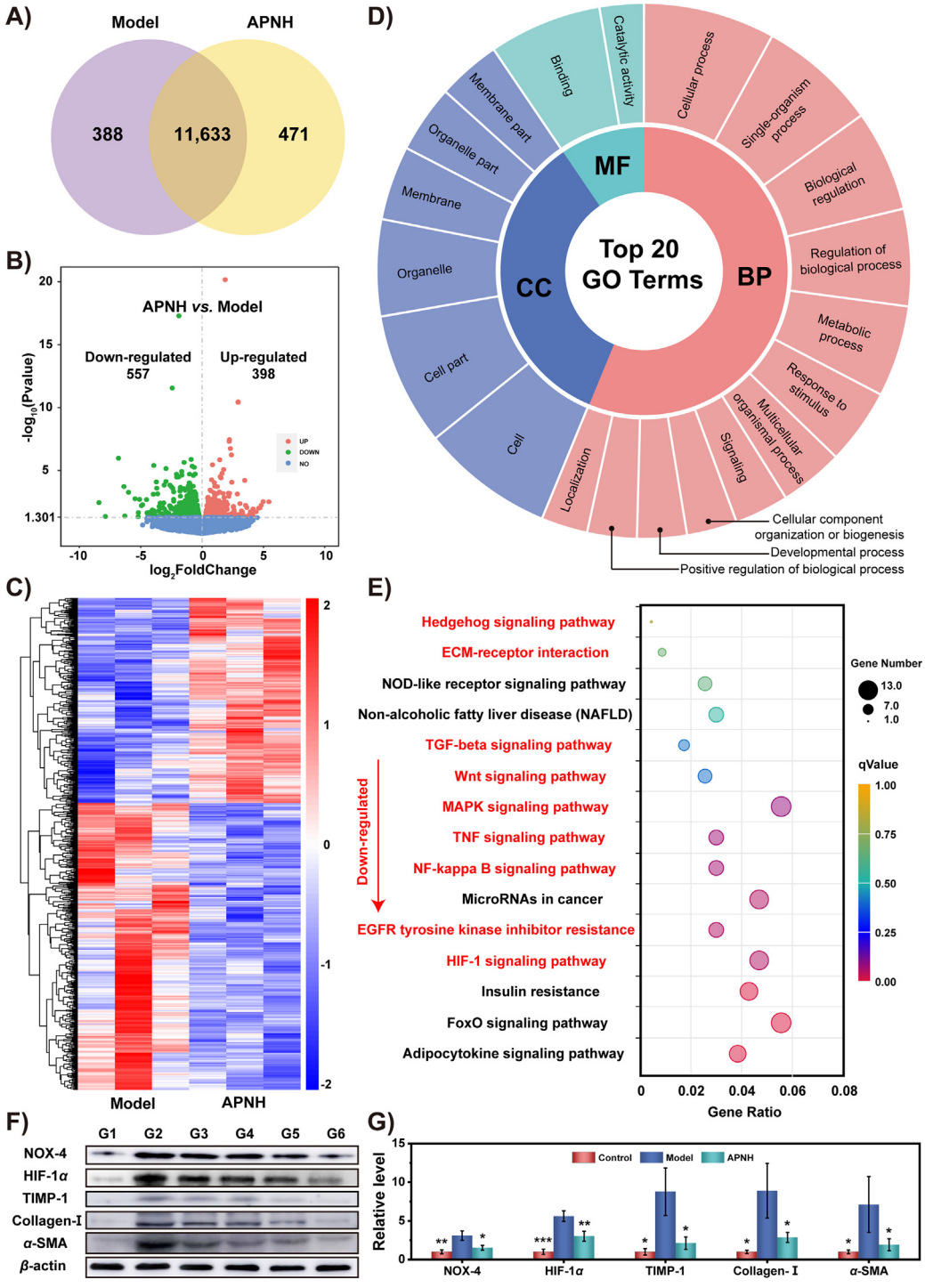

Figure 8 Molecular mechanism of the therapeutic activity of APNH NTs *in vivo*. (A) Venn diagram prepared from the liver transcriptomic profiles determined in APNH NTs and model cohorts. (B) Volcano plot exhibiting the up- and downregulated genes in the APNH NTs cohort compared with the model group. (C) Heatmap showing the DEGs identified in the livers of the model and APNH NTs cohorts. (D) GO annotation of all DEGs identified in the APNH NTs group *vs.* the model group. BP: biological process; CC: cellular component; MF: molecular function. (E) KEGG pathways that were downregulated due to APNH NTs administration (compared to the model cohort). The pathways labeled in red are closely related to the antifibrogenic/enzymomimetic activity of APNH NTs and their inhibitory activity toward the activation of HSCs. (F) Western blotting analysis of the protein expression of NOX-4, HIF-1α, TIMP-1, collagen-I and α-SMA in the livers collected from different groups. G1: control, G2: model, G3: Ag@Pt NTs, G4: NIL, G5: APNH NTs (low dose), and G6: APNH NTs (high dose). (G) Densitometric analysis of the western blotting results. Data are shown as the mean ± SD ($n = 3$). NS (no significance), $^{*}P < 0.05$, $^{**}P < 0.01$, $^{***}P < 0.001$.

differential transcriptomic profiles between the model and APNH NTs cohorts (Supporting Information Fig. S41). Additional data processing of the DEGs revealed that multiple genes and their associated pathways are involved in liver fibrogenesis. Therefore, to further delineate the molecular mechanisms responsible for APNH NTs activity, we employed the second and third-level Gene Ontology (GO) terms and identified DEGs that were enriched in the top 20 GO terms belonging to various biological processes (BPs), cellular components (CCs) or molecular functions (MFs) (Fig. 8D). It is worth noting that a plethora of DEGs were involved in catalytic activity, metabolic processes, response to stimuli and biological regulation, which is in line with the designed properties of APNH NTs. Moreover, the kyoto encyclopedia of genes and genomes (KEGG) enrichment analysis was conducted to assess the molecular pathways affected by APNH NTs administration. As shown in Fig. 8E, KEGG analysis revealed 15 downregulated pathways. Among them, multiple pathways closely related to liver fibrosis were identified, highlighting the multimodal antifibrogenic activity of APNH NTs. Interestingly, the APNH NTs-treated group exhibited extensive downregulation of the MAPK, TGF-β, NF-κB, Wnt and Hedgehog signaling pathways. All of these pathways have been previously determined to be positively correlated with the activation of HSCs and liver fibrogenesis[43,44]. In addition, downregulation of the TNF signaling pathway, ECM-receptor interactions and EGFR tyrosine kinase inhibitor resistance further confirmed the ability of APNH NTs to induce collagen depletion[45]. Importantly, the HIF-1 signaling pathway was also significantly downregulated, which is plausibly due to the SOD and CAT-like activities of APNH NTs. Hypoxia accelerates liver fibrosis by mediating chronic inflammation and collagen deposition. HIF-1, an important transcription factor regulating oxygen metabolism, plays an important role in liver fibrogenesis[46]. Under hypoxic conditions, HIF-1 can promote liver fibrosis by regulating the expression of TIMP-1, which is a downstream target of HIF-1[47]. Therefore, we finally investigated the expression levels of NOX-4, HIF-1α, TIMP-1, collagen-I and α-SMA in the livers of treated mice (Fig. 8F and G). Compared to the model fibrotic group, the expression levels of these proteins decreased significantly due to APNH NTs exposure. Importantly, this is consistent with the transcriptomics results discussed above. Taken together, these results illustrated that APNH NTs regulate multiple signaling pathways by simultaneously remodeling the microenvironment of liver fibrosis and inhibiting HSCs activation with a highly boosted antifibrogenic effect.

3.8. *Metabolism and biosafety of APNH NTs in vivo*

For the metabolism study, a decay equation was constructed to determine the metabolic degradation of APNH NTs, obtaining the fitted Eq. (1) for Ag and Eq. (2) for Pt (Supporting Information Figs. S42A and S42B):

$$y = 18.12\exp(-t/1.93) + 17.71\exp(-t/1.93 - 0.03 \quad (1)$$

$$y = 68.61\exp(-t/1.35) + 64.82\exp(-t/1.35) + 0.91 \quad (2)$$

In addition, we aimed to delineate the preferential excretion route of APNH NTs. As shown in Figs. S42C and S42D, APNH NTs were excreted by urine and feces, reaching the maximum amount between 6 and 12 h after intravenous injection. Although the Ag and Pt elements were detected in both urine and feces, fecal excretion was the predominant route. Furthermore, the bioaccumulation of APNH NTs was investigated by quantifying the total amounts of Ag and Pt in organ mass. As illustrated in Figs. S42E and S42F, owing to the liver targeting ability of APNH NTs, Ag and Pt were mainly detected in the liver and reached 7.27% and 19.94% ID/g at 12 h, respectively. These results indicated that the biodistribution of Ag and Pt was close to 0.36/1, which is in agreement with the EDS results (27.83%:72.17% = 0.39/1).

Finally, we investigated the possible side effects of APNH NTs, including alteration of the typical biochemical parameters in serum and unwanted histopathological features in H&E-stained tissues. Compared to the control and model groups, the hepatic and renal functions did not exhibit a significant change in any of the APNH NTs-treated groups (Supporting Information Fig. S43). This indicates no observable hepatotoxicity or nephrotoxicity caused by APNH NTs. This finding was further corroborated by H&E staining, which demonstrated no pathological features in the APNH NTs-treated cohorts (Supporting Information Fig. S44). Taken together, the obtained data revealed excellent long-term biosafety, even at the maximum dose of APNH NTs.

4. Conclusions

In summary, we successfully designed and tested the use of APNH NTs as a synergetic multimodal strategy for attenuating liver fibrosis. The core of the APNH NTs, Ag@Pt bimetallic nanozymes, possessed outstanding ROS scavenging ability, which enabled a significant decrease in hepatic HSCs activation. Importantly, multicatalytic enzymomimetic Ag@Pt nanozymes catalyzed H_2O_2 decomposition to produce O_2, resulting in hypoxia alleviation by suppressing HIF-1α expression. Moreover, NIL was released from the APNH NTs in a pH-responsive manner to promote extracellular collagen depletion, thus synergistically remodeling the microenvironment of liver fibrosis. Comprehensive *in vitro* and *in vivo* experiments demonstrated that APNH NTs treatment effectively alleviated liver fibrosis. Importantly, the RNA-Seq analysis revealed that the molecular mechanisms of APNH NTs therapy were related to multiple signaling pathways, including the HIF-1, NF-κB, TNF, MAPK, Wnt, and TGF-β signaling pathways. Overall, the presented results demonstrate the effectiveness of APNH NTs as a novel multimodal therapeutic agent with exceptional antifibrogenic activity and provide a highly promising strategy for the treatment of liver fibrosis.

Acknowledgments

This work was supported by the Young Elite Scientists Sponsorship Program by Tianjin (No. 0701320001, China), Major Special Projects (No. 0402080005, China), National Key R&D Program of China (No. 2020YFC1512304, China) and National Natural Science of China (Nos. 82273873, 31971106, and 81372124, China) and the Czech Health Council (AZV NU12J-08−00043, Czech). Moreover, we express our gratitude to Zhi Li (School of Pharmaceutical Science and Technology, Tianjin University, China) for the assistance in the FACS experiments.

Author contributions

Nan Li, Vojtech Adam and Huaqing Jing designed the research. Huaqing Jing, Yue Zhou and Yingzi Ren carried out the experiments and performed data analysis. Min Xu, Qiang Lu, Siyu Wang

and Xiaoyang Liang participated part of the experiments. Huaqing Jing wrote the manuscript. Sona Krizkova and Zbynek Heger polished and revised the manuscript. All of the authors have read and approved the final manuscript.

Conflicts of interest

The authors have no conflicts of interest to declare.

Appendix A. Supporting information

Supporing data to this article can be found online at https://doi.org/10.1016/j.apsb.2023.08.020.

References

1. Kisseleva T, Brenner D. Molecular and cellular mechanisms of liver fibrosis and its regression. *Nat Rev Gastroenterol Hepatol* 2021;**18**:151–66.
2. Wynn TA, Ramalingam TR. Mechanisms of fibrosis: therapeutic translation for fibrotic disease. *Nat Med* 2012;**18**:1028–40.
3. Krenkel O, Tacke F. Liver macrophages in tissue homeostasis and disease. *Nat Rev Immunol* 2017;**17**:306–21.
4. Pellicoro A, Ramachandran P, Iredale JP, Fallowfield JA. Liver fibrosis and repair: immune regulation of wound healing in a solid organ. *Nat Rev Immunol* 2014;**14**:181–94.
5. Mehal WZ, Iredale J, Friedman SL. Scraping fibrosis: expressway to the core of fibrosis. *Nat Med* 2011;**17**:552–3.
6. Schuppan D, Kim YO. Evolving therapies for liver fibrosis. *J Clin Invest* 2013;**123**:1887–901.
7. Zhang CY, Yuan WG, He P, Lei JH, Wang CX. Liver fibrosis and hepatic stellate cells: etiology, pathological hallmarks and therapeutic targets. *World J Gastroenterol* 2016;**22**:10512–22.
8. Rockey DC, Bell PD, Hill JA. Fibrosis—a common pathway to organ injury and failure. *N Engl J Med* 2015;**372**:1138–49.
9. Copple BL, Bai S, Burgoon LD, Moon JO. Hypoxia-inducible factor-1 alpha regulates the expression of genes in hypoxic hepatic stellate cells important for collagen deposition and angiogenesis. *Liver Int* 2011;**31**:230–44.
10. Foglia B, Novo E, Protopapa F, Maggiora M, Bocca C, Cannito S, et al. Hypoxia, hypoxia-inducible factors and liver fibrosis. *Cells* 2021;**10**:1764.
11. Bataller R, Brenner DA. Hepatic stellate cells as a target for the treatment of liver fibrosis. *Semin Liver Dis* 2001;**21**:437–51.
12. Prakash J, Pinzani M. Fibroblasts and extracellular matrix: targeting and therapeutic tools in fibrosis and cancer Preface. *Adv Drug Deliv Rev* 2017;**121**:1–2.
13. Roderfeld M. Matrix metalloproteinase functions in hepatic injury and fibrosis. *Matrix Biol* 2018;**68–69**:452–62.
14. Weiskirchen R. Hepatoprotective and anti-fibrotic agents: it's time to take the next step. *Front Pharmacol* 2016;**6**:303.
15. Shiha GE, Abu-Elsaad NM, Zalata KR, Ibrahim TM. Tracking anti-fibrotic pathways of nilotinib and imatinib in experimentally induced liver fibrosis: an insight. *Clin Exp Pharmacol Physiol* 2014;**41**:788–97.
16. Liu YQ, Wang Z, Kwong SQ, Lui ELH, Friedman SL, Li FR, et al. Inhibition of PDGF, TGF-beta, and Abl signaling and reduction of liver fibrosis by the small molecule Bcr-Abl tyrosine kinase antagonist Nilotinib. *J Hepatol* 2011;**55**:612–25.
17. Andersson P, Von Euler M, Beckert M. Comparable pharmacokineties of 85 mg RightSize nilotinib (XS003) and 150 mg Tasigna in healthy volunteers using a hybrid nariopartick-based formulation platform for protein kinase inhibitors. *J Clin Oncol* 2014;**32**:1.
18. Qiao JB, Fan QQ, Xing L, Cui PF, He YJ, Zhu JC, et al. Vitamin A-decorated biocompatible micelles for chemogene therapy of liver fibrosis. *J Control Release* 2018;**283**:113–25.
19. Lin LT, Gong HY, Li R, Huang JJ, Cai MY, Lan T, et al. Nanodrug with ROS and pH dual-sensitivity ameliorates liver fibrosis *via* multicellular regulation. *Adv Sci* 2020;**7**:1903138.
20. Wu PK, Luo XP, Wu H, Zhang QY, Dai YX, Sun MJ. Efficient and targeted chemo-gene delivery with self-assembled fluoro-nanoparticles for liver fibrosis therapy and recurrence. *Biomaterials* 2020;**261**:120311.
21. Qiao JB, Fan QQ, Zhang CL, Lee J, Byun J, Xing L, et al. Hyperbranched lipoid-based lipid nanoparticles for bidirectional regulation of collagen accumulation in liver fibrosis. *J Control Release* 2020;**321**:629–40.
22. Xu YC, Chen J, Jiang W, Zhao YY, Yang C, Wu Y, et al. Multiplexing nanodrug ameliorates liver fibrosis *via* ROS elimination and inflammation suppression. *Small* 2022;**18**:e2102848.
23. Liu R, Luo C, Pang Z, Zhang J, Ruan S, Wu M, et al. Advances of nanoparticles as drug delivery systems for disease diagnosis and treatment. *Chin Chem Lett* 2023;**34**:107518.
24. Lu Q, Zhou Y, Xu M, Liang XY, Jing HQ, Wang XX, et al. Sequential delivery for hepatic fibrosis treatment based on carvedilol loaded star-like nanozyme. *J Control Release* 2022;**341**:247–60.
25. Tabbasam R, Khursid S, Ishaq Y, Malik A. *In vivo* evaluation of inorganic nanoparticle complexes against CCL4 induced hepatotoxicity. *Curr Drug Deliv* 2021;**18**:1197–203.
26. Liu YF, Cheng Y, Zhang H, Zhou M, Yu YJ, Lin SC, et al. Integrated cascade nanozyme catalyzes *in vivo* ROS scavenging for anti-inflammatory therapy. *Sci Adv* 2020;**6**:eabb2695.
27. Qi GH, Zhang Y, Wang JF, Wang DD, Wang B, Li HJ, et al. Smart plasmonic nanozyme enhances combined chemo-photothermal cancer therapy and reveals tryptophan metabolic apoptotic pathway. *Anal Chem* 2019;**91**:12203–11.
28. Nambara K, Niikura K, Mitomo H, Ninomiya T, Takeuchi C, Wei JJ, et al. Reverse size dependences of the cellular uptake of triangular and spherical gold nanoparticles. *Langmuir* 2016;**32**:12559–67.
29. Li WH, Zhou CC, Fu Y, Chen TJ, Liu X, Zhang ZR, et al. Targeted delivery of hyaluronic acid nanomicelles to hepatic stellate cells in hepatic fibrosis rats. *Acta Pharm Sin B* 2020;**10**:693–710.
30. Zhang Q, Li N, Goebl J, Lu Z, Yin Y. A systematic study of the synthesis of silver nanoplates: is citrate a "magic" reagent?. *J Am Chem Soc* 2011;**133**:18931–9.
31. Popa A, Samia AC. Effect of metal precursor on the growth and electrochemical sensing properties of Pt-Ag nanoboxes. *Chem Commun* 2014;**50**:7295–8.
32. Fan QQ, Zhang CL, Qiao JB, Cui PF, Xing L, Oh YK, et al. Extracellular matrix-penetrating nanodrill micelles for liver fibrosis therapy. *Biomaterials* 2020;**230**:119616.
33. Parola M, Robino G. Oxidative stress-related molecules and liver fibrosis. *J Hepatol* 2001;**35**:297–306.
34. Wu XX, Wu XD, Ma YX, Shao F, Tan Y, Tan T, et al. CUG-binding protein 1 regulates HSC activation and liver fibrogenesis. *Nat Commun* 2016;**7**:13498.
35. Ebrahimi H, Naderian M, Sohrabpour AA. New concepts on reversibility and targeting of liver fibrosis; a review. *Middle East J Dig Dis* 2018;**10**:133–48.
36. Koyama Y, Xu J, Liu X, Brenner DA. New developments on the treatment of liver fibrosis. *Dig Dis* 2016;**34**:589–96.
37. Lambeth JD. Nox enzymes, ROS, and chronic disease: an example of antagonistic pleiotropy. *Free Radic Biol Med* 2007;**43**:332–47.
38. Mortezaee K. Nicotinamide adenine dinucleotide phosphate (NADPH) oxidase (NOX) and liver fibrosis: a review. *Cell Biochem Funct* 2018;**36**:292–302.
39. Crosas-Molist E, Fabregat I. Role of NADPH oxidases in the redox biology of liver fibrosis. *Redox Biol* 2015;**6**:106–11.
40. Hu CJ, Wang LY, Chodosh LA, Keith B, Simon MC. Differential roles of hypoxia-inducible factor 1 alpha (HIF-1 alpha) and HIF-2 alpha in hypoxic gene regulation. *Mol Cell Biol* 2003;**23**:9361–74.
41. Fujii T, Fuchs BC, Yamada S, Lauwers GY, Kulu Y, Goodwin JM, et al. Mouse model of carbon tetrachloride induced liver fibrosis:

histopathological changes and expression of CD133 and epidermal growth factor. *BMC Gastroenterol* 2010;**10**:79.
42. Dai Y, Xu C, Sun X, Chen X. Nanoparticle design strategies for enhanced anticancer therapy by exploiting the tumour microenvironment. *Chem Soc Rev* 2017;**46**:3830−52.
43. Gan GN, Jimeno A. Emerging from their burrow: hedgehog pathway inhibitors for cancer. *Expet Opin Invest Drugs* 2016;**25**:1153−66.
44. Duspara K, Bojanic K, Pejic JI, Kuna L, Kolaric TO, Nincevic V, et al. Targeting the Wnt signaling pathway in liver fibrosis for drug options: an update. *J Clin Transl Hepatol* 2021;**9**:960−71.
45. Khanjarsim V, Karimi J, Khodadadi I, Mohammadalipour A, Goodarzi MT, Solgi G, et al. Ameliorative effects of nilotinib on CCl4 induced liver fibrosis *via* attenuation of RAGE/HMGB1 gene expression and oxidative stress in rat. *Chonnam Med J* 2017;**53**:118−26.
46. Rosmorduc O, Housset C. Hypoxia: a link between fibrogenesis, angiogenesis, and carcinogenesis in liver disease. *Semin Liver Dis* 2010;**30**:258−70.
47. Mochizuki A, Pace A, Rockwell CE, Roth KJ, Chow A, O'Brien KM, et al. Hepatic stellate cells orchestrate clearance of necrotic cells in a hypoxia-inducible factor-1 alpha-dependent manner by modulating macrophage phenotype in mice. *J Immunol* 2014;**192**:3847−57.